

Multimessenger constraints on outflows from neutron star mergers

A thesis submitted
in partial fulfillment for the award of the degree of

Master of Science

in

Astronomy and Astrophysics

by

B.S.Bharath Saiguhan



Department of Earth and Space Sciences
Indian Institute of Space Science and Technology
Thiruvananthapuram, India

June 10, 2021

Certificate

This is to certify that the thesis titled *Multimessenger constraints on outflows from neutron star mergers* submitted by **B.S.Bharath Saiguhan**, to the Indian Institute of Space Science and Technology, Thiruvananthapuram, in partial fulfillment for the award of the degree of **Master of Science in Astronomy and Astrophysics** is a bona fide record of the original work carried out by him under my supervision. The contents of this thesis, in full or in parts, have not been submitted to any other Institute or University for the award of any degree or diploma.

Dr. Resmi Lekshmi
Designation

Name of Department Head
Designation

Place: Thiruvananthapuram
Date: June 10, 2021

Declaration

I declare that this thesis titled *Multimessenger constraints on outflows from neutron star mergers* submitted in partial fulfillment for the award of the degree of **Master of Science in Astronomy and Astrophysics** is a record of the original work carried out by me under the supervision of **Dr. Resmi Lekshmi**, and has not formed the basis for the award of any degree, diploma, associateship, fellowship, or other titles in this or any other Institution or University of higher learning. In keeping with the ethical practice in reporting scientific information, due acknowledgments have been made wherever the findings of others have been cited.

Place: Thiruvananthapuram

B.S.Bharath Saiguhan

Date: June 10, 2021

(SC16B123)

Acknowledgements

I would like to thank my parents for the unparalleled support and encouragement they have provided over the years, as well as in the year in which this work was carried out. I wouldn't be here without their words of affection and wisdom, and I cannot thank them enough.

I would also like to thank Dr. R. Lekshmi for the ceaseless guidance and for the keen insight into the problems faced along the way. With her ready assistance and patience carrying out this project, even if remotely, was engaging and rewarding.

Additionally, I would like to thank Dr. K. G. Arun at the Chennai Mathematical Institute in Tamilnadu, India and Dr. M. Saleem at the University of Minnesota in Minneapolis, United States for their contributions and for guidance in this work. I would also like to thank Dr. B. S. Sathyaprakash, at the Pennsylvania State University, University Park, United States for his invaluable inputs and constructive remarks on the arguments developed here, which greatly helped to structure and refine this work.

In addition, I would also like to thank the support staff at IIST, especially Mr. Sai Krishnan at the Astronomy Lab, who has helped greatly specially in the setup and maintenance of the remote access node to workstations at IIST.

I would also like to thank Ms. Aashka Oza for her excellent suggestions which helped improve the presentation and the flow of this report greatly. Additionally, I would like to thank her for the tremendous support and inspiration that she has given me during the entire course of my time at IIST. My life has been richer with her amazing *joie de vivre* and infallible companionship.

Furthermore, I would also like to acknowledge the tremendous contributions of the libre and open source community via their core utilities and tools. Without the natural suitability of these tools for scientific workflows and excellent text editing support of Vim, this body of work would have been an unnecessarily herculean task.

Finally, I would like to acknowledge the immense efforts of those who have risked their lives during such unprecedeted times for the benefit of others, and to ensure that essential services and societal infrastructures still operate.

B.S.Bharath Saiguhan

Abstract

Abstract here.

Contents

| | |
|---|-------------|
| List of Figures | xi |
| List of Tables | xiii |
| Abbreviations | xv |
| 1 Introduction | 1 |
| 1.1 Outflows from BNS Mergers | 1 |
| 1.2 Outflows from NSBH Mergers | 7 |
| 1.3 NS mergers in GW regime | 16 |
| 1.4 Summary | 18 |
| 2 Population Synthesis | 19 |
| 2.1 Black Hole Population Models | 19 |
| 2.2 Neutron Star Population Models | 23 |
| 2.3 Spatial Distribution and Orientation of Samples | 24 |
| 2.4 Validation of Population Synthesis Code | 26 |
| 2.5 Summary | 33 |
| 3 NS Merger Candidates in GWTC-2 | 35 |
| 3.1 About GWTC-2 | 35 |
| 3.2 Analysis of GW190425 | 39 |
| 3.3 Preliminary analysis of GW190426_152155 | 48 |
| 3.4 Summary | 52 |
| 4 Event and Population Analysis | 53 |
| 4.1 Analysis of Population Synthesis Models | 53 |
| 4.2 Event Analysis | 56 |

| | | |
|-------------------|-------------------------------|-----------|
| 4.3 | Summary | 63 |
| 5 | Results and Discussion | 65 |
| 5.1 | Summary | 65 |
| References | | 66 |

List of Figures

| | | |
|------|---|----|
| 1.1 | Relative Positions of Jet Delays | 4 |
| 1.2 | Tophat jet structure model | 5 |
| 1.3 | Jet structures as in Hayes et al. 2020 | 6 |
| 1.4 | Disruption condition in a NSBH binary | 9 |
| 1.5 | Rest mass outside black hole horizon, as a function of time | 9 |
| 1.6 | Tidal disruption of a NS in a 3:1 NSBH binary | 10 |
| 1.7 | Tidal disruption of a NS in a 5:1 NSBH binary | 10 |
| 2.1 | Black hole mass distribution with upper limit | 20 |
| 2.2 | Black hole mass distributions from GWTC-2 | 21 |
| 2.3 | Black hole spin distribution from GWTC-2 | 22 |
| 2.4 | Uniform Black Hole Spin Distribution | 22 |
| 2.5 | Gaussian Black Hole Spin Distributions | 23 |
| 2.6 | Distribution of GW network SNR | 28 |
| 2.7 | $D_L - \iota$ correlation in the population | 29 |
| 2.8 | Validation of the jet structure code | 30 |
| 2.9 | Variation of $\mathcal{N}(> \mathcal{F})$ with \mathcal{F} | 31 |
| 2.10 | Variation of $\mathcal{F}(\chi_{BH}, \theta_v)$ for a $\mathcal{Q} = 3 : 1.4$ NSBH binary merger | 32 |
| 2.11 | Variation of $\mathcal{F}(\chi_{BH}, \theta_v)$ for a $\mathcal{Q} = 5 : 1.4$ NSBH binary merger | 33 |
| 2.12 | Variation of $\mathcal{F}(\chi_{BH}, \theta_v)$ for a $\mathcal{Q} = 10 : 1.4$ NSBH binary merger | 34 |
| 3.1 | $D_L - \iota$ Posterior distribution. | 42 |
| 3.2 | Variation of the apparent isotropic equivalent energy, for observers at different viewing angles | 43 |
| 3.3 | Broken power law distribution from Ghirlanda et al. 2016. | 44 |
| 3.4 | Posterior distributions of the $E_{iso}(0)$, for two assumed priors on $E_{tot,\gamma}$ | 46 |
| 3.5 | $D_L - \iota$ posterior, with samples from the data released by LVC. | 47 |

| | | |
|-----|---|----|
| 3.6 | Posterior distributions of $E_{iso}(0)$ with similar priors as Fig. 3.4, but with LVC posterior samples as input. | 48 |
| 3.7 | Posterior distributions of $E_{iso}(0)$, in the case of GW190426_152155. | 49 |
| 4.1 | Variation of M_{disc} with χ_{BH} and \mathcal{Q} | 56 |
| 4.2 | GW190426 in the $\chi_{BH} - \mathcal{Q}$ plane | 58 |
| 4.3 | EM outflows from NSBH mergers, from Barbieri, Salafia, Perego, et al. 2019 | 59 |
| 4.4 | M_{disc} for GW170817’s Low Spin Posterior Distribution | 60 |
| 4.5 | M_{disc} for GW170817’s High Spin Posterior Distribution | 61 |
| 4.6 | M_{disc} for GW190425’s Low Spin Posterior Distribution | 62 |
| 4.7 | M_{disc} for GW190425’s High Spin Posterior Distribution | 63 |

List of Tables

| | | |
|-----|--|----|
| 3.1 | Candidate Merger Events and GRACE-DB Superevent IDs | 37 |
| 3.2 | Candidate Merger Events and FARs | 38 |
| 3.3 | Candidate merger events and relevant GCNs | 39 |
| 3.4 | Priors on $E_{tot,\gamma}$, Γ_0 and θ_c | 44 |
| 3.5 | List of typical cosmological SGRBs and their source parameters . . . | 51 |
| 4.1 | Number and Kind of Detections across Population Classes | 55 |

Abbreviations

| | |
|----------|--|
| ACS | Anti-Coincidence Shield (onboard the INTEGRAL satellite) |
| BAT | Burst-Alert Telescope (onboard the Swift satellite) |
| BBH | Binary Black Hole (as in binary, merger) |
| BNS | Binary Neutron Star (as in binary, merger) |
| CBC | Compact Binary Coalescence |
| EM | Electromagnetic (as in waves, spectrum) |
| FIF | Fisher Information Formalism |
| FIM | Fisher Information Matrix |
| GBM | Gamma-ray Burst Monitor (onboard the FERMI satellite) |
| GCN | Gamma-ray burst Coordinates Network |
| GRACE-DB | GRAvitational-wave Candidate Event DataBase |
| GW | Gravitational Waves |
| GWTC | Gravitational Wave Transient Catalog |
| INTEGRAL | INTERnational Gamma-Ray Astrophysics Laboratory |
| ISCO | Innermost Stable Circular Orbit (of a black hole) |
| LHO, H1 | LIGO Hanford Observatory |
| LIGO | Laser Interferometer Gravitational-wave Observatory |
| LLO, L1 | LIGO Livingston Observatory |
| LSC | LIGO Scientific Collaboration |
| LVC | LIGO-Virgo Collaboration |
| MRI | Magneto-Rotational Instability |
| NSBH | Neutron Star Black Hole (as in binary, merger) |
| O3a | Observing run 3a (as in first half of 3rd run) |
| PN | Post-Newtonian |
| PSD | Power Spectral Density |
| RWF | Restricted Wave Form |
| SAA | South Atlantic Anomaly |

| | |
|------|----------------------------|
| SGRB | Short Gamma-Ray Burst |
| SNR | Signal-to-Noise Ratio |
| UTC | Universal Coordinated Time |
| V1 | VIRGO Observatory |

Chapter 1

Introduction

1.1 Outflows from BNS Mergers

Due to the joint electromagnetic and gravitational wave detection of the binary neutron star merger event GW170817 (see B. P. Abbott et al. 2018), there has been renewed interest in SGRBs. Specifically, this detection gives credence to the claim that the central engines of SGRBs are binary neutron star mergers (see Narayan, Paczynski, and Piran 1992). There are however other aspects of the process that are not as clear. In particular, several aspects of GW170817 have not been completely explained. The main concerns are as follows (Lazzati 2020):

- The outflow of GRB170817A (the gamma-ray counterpart event to GW170817) was lower in energy than a typical cosmological SGRB, by a factor of $10^4 - 10^5$, even though the event was one of the closest GW events recorded, at a distance of ~ 40 Mpc. The reasons for this could be twofold:
 - The structured jet was viewed off-axis with respect to the observer.
 - The internal engine powering this SGRB was intrinsically less energetic, and differs from the one observed in other typical SGRBs.
- A clear consensus has not been reached on *how* the gamma-ray prompt emission was produced. Models which have been considered to explain the jet launching include :
 - The structured outflow model, characterised by functions for the Lorentz factor and the energy per unit solid angle, both of which vary with the angle made with the polar jet axis, θ . This model produces detectable signals even at moderately large off-axis angles.

- The shock breakout model (Gottlieb et al. 2018), wherein the leading edge of the wind emits the prompt emission as it breaks out of the cocoon of nuclear matter ejected before the jet was launched. This model has been shown to explain the energetics and spectrum of the prompt emission, although it does require a setup in which the wind is fast enough so that it can reach a large enough distance at breakout.

The uncertainty in the jet production mechanism partly comes from the fact that the various delays which play major roles *before* the observation of the prompt emission have not been accurately constrained, although rough estimates for each component exist.

More light can be shed on these questions by observing more such SGRBs, using both the gravitational wave (GW) and electromagnetic (EM) windows. However, the possibility of joint detections are slim, due to the fact that the EM observations are highly dependent on the viewing angle of the system with respect to the observer (due to relativistic beaming), whereas GW signal amplitudes depend on the distance to the event (see Seto 2015).

Given that this is the case, it would be expedient to look for constraints on the structure parameters of various models. Furthermore, it would be ideal to develop models which are resilient to *non*-detections, i.e. those that can produce constraints on the parameters using even upper limits on the flux/fluence observed by the various EM follow-up satellites, such as INTEGRAL, FERMI-GBM or Swift/BAT. For this purpose, the structured jet model is adopted in this report and used as a starting point. Using this model as a springboard, the properties of prompt emissions from NS mergers are investigated.

1.1.1 Modelling outflows from BNS Mergers

As mentioned before, the electromagnetic follow-up of the binary neutron star merger event GW170817 helped (roughly) measure the various time delays between the time of the GW signal trigger (which roughly is the merger time itself) and the time the gamma-ray signals were picked up. This time delay is denoted $\Delta t_{GW-\gamma}$, and was around 1.75 seconds for this event. The components which make up this delay are as follows (Lazzati 2020):

- **Engine Delay** – this is the delay due to a transition in the central engine mechanism which powers the jet. For example, such a transition could be a metastable, fast spinning neutron star collapsing, post-merger, into a black hole when its rotation period increases (a process that can take years). Or it could be the time elapsed in amplifying the magnetic field to a value large enough for jet launching (a process which is significantly faster, taking only seconds). This delay is denoted by Δt_{eng} .
- **Wind Delay** – this is simply a delay in the launching of a non-relativistic wind due to the neutron-rich matter from the progenitor(s) being tidally shredded. For this reason, it can be *negative* as well, since the tidal shredding can occur before the merger itself. This is denoted as Δt_{wind} .
- **Breakout Delay** – if the wind is ejected before the jet, then the latter will have to propagate through the former. This happens at a sub-relativistic speed, whereas the GW signal travels at a relativistic speed. The delay due to this crossing is the breakout delay, and is denoted Δt_{BO} . During this time, jet-wind interactions cause the development of a structured outflow that maintains a bright core but also has energetic wings at large polar angles.
- **Photospheric Delay** – once the jet has crossed the wind, it still needs to propagate out to the photospheric radius, where the outflow becomes transparent and the prompt gamma-ray emission is radiated. The delay from the breakout radius to the photospheric radius is Δt_{ph} . For GW170817, this is given by:

$$\Delta t_{ph} \sim \frac{R_{ph}}{c\Gamma^2} = 1.4 \frac{R_{ph}}{2 \times 10^{12} \text{ cm}} \left(\frac{7}{\Gamma}\right)^2 \text{ s} \quad (1.1)$$

- **Dissipation Delay** – this is a requirement in some models, such as the internal shock synchrotron model, wherein the outflow needs to travel to the internal shock radius before the bulk energy of the flow is dissipated and turned into radiation. The time required to get to this point after crossing the photospheric radius is the dissipation delay, denoted Δt_γ

Several attempts to constrain the various time delay components have been made. However, no conclusions have been arrived upon except for relative comparisons. For example, one can only say that the photospheric delay is the major component out of all the delays, and that wind delay (if non-zero) has to be lesser than the jet delay,

so that the jet catches up to the wind and the jet-wind interaction generates the structured outflow. Fig. 1.1 summarises these delays in the broader context.

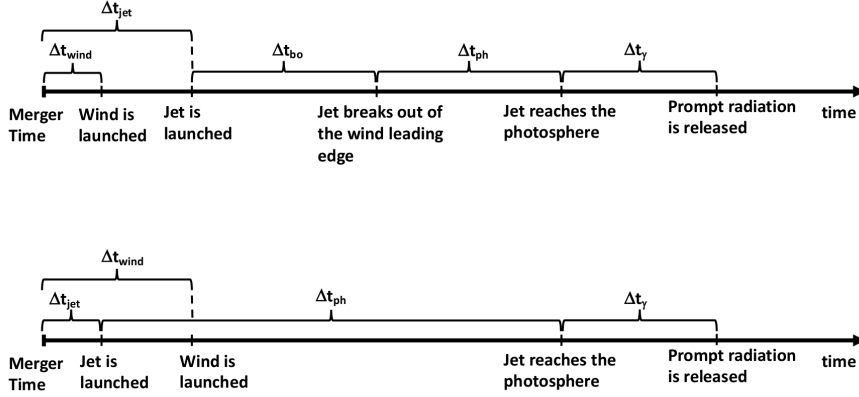


Figure 1.1: Two possible scenarios for the relative positioning of the delays in time, which contribute to $\Delta t_{GW-\gamma}$. Owing to the requirement of a structured outflow, GW170817 possibly follows the top timeline. The relative contributions of the various delays are debated, but it is agreed that $\Delta t_{wind} < \Delta t_{jet} \ll 1$ s, $\Delta t_{BO} \ll 1$ s, $\Delta t_\gamma \sim 0$ and $\Delta t_{ph} \sim \Delta t_{GW-\gamma}$.

Due to the uncertainties in the delay terms, several models for the jet can explain the energetics and observed structure. Numerical simulations are also unequivocal about their favouring of one model over the other (see Shibata and Hotokezaka 2019). Some models try to explain the *apparent* structure of the jet, which are the observables seen by a particular observer at a particular viewing angle. Other models are used to explain the *intrinsic* structure, such as the polar angle variation of the bulk Lorentz factor and the energy across the solid angle, in the jet co-moving frame. See Salafia et al. 2015 for a detailed discussion of the differences between the two structures. Some of the models considered are described below (see also Figs. 1.2 and 1.3):

- Top-hat – This model, as used in M. Saleem et al. 2020, assumes that the bulk Lorentz and energy functions drop to zero beyond some cutoff angle, θ_j . Below this threshold, the functions are at their respective on-axis values.
- Gaussian – This model is widely used, in some contexts to explain the apparent jet structure (by Hayes et al. 2020), and in others the intrinsic jet structure (by M. Saleem et al. 2020). The former is simply given by $y_{GJ}(\theta) = e^{-\frac{1}{2}\left(\frac{\theta}{\theta_\sigma}\right)^2}$, since the authors consider only the apparent jet structure, as explained above and

θ_σ is a structure parameter which is inferred by the authors' Bayesian inference code.

In the latter, as the authors consider the intrinsic jet structure, they assume that $\Gamma\beta(\theta) = \Gamma_0\beta_0 \exp(-\theta^2/2\theta_c^2)$ and that $\epsilon(\theta) \propto \exp(-\theta^2/\theta_c^2)$ ¹, and derive the observed properties (see below).

- Power Law – This model is used by Hayes et al. 2020 to explain the apparent structure of the jet, assuming that any variation in the energy is simply because of relativistic beaming and the jet being viewed off-axis. It is given using the shape function $y(\theta)$ (which is multiplied with the on-axis isotropic equivalent energy $E_{iso,0}$ to give $E_{iso}(\theta)$)²:

$$y(\theta) = \begin{cases} 1, & 0 \leq \theta \leq \theta_c, \\ (\theta/\theta_c)^{-2}, & \theta_c < \theta \leq \theta_j, \\ 0, & \theta_j < \theta \end{cases} \quad (1.2)$$

Here θ_c and θ_j are simply structure parameters, inferred using Bayesian methods.

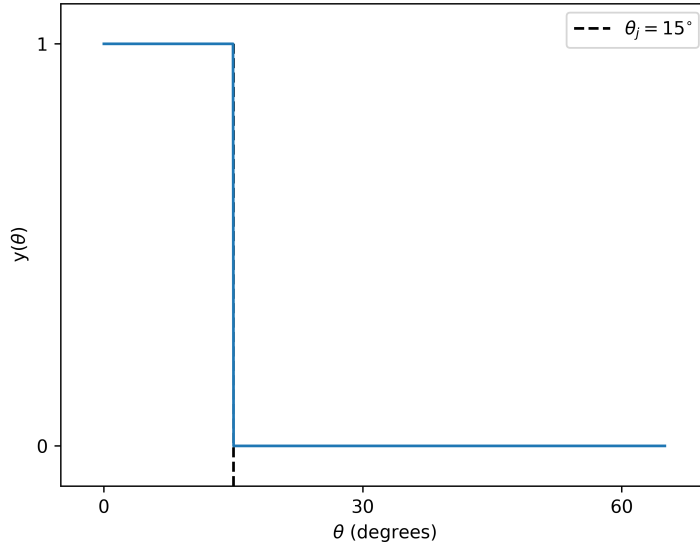


Figure 1.2: Functional form of the tophat jet structure model, as considered in M. Saleem et al. 2020. The dashed line denotes the jet angle $\theta_j = 15^\circ$.

¹This is the normalised energy profile function. The normalisation constant is estimated by the condition $2\pi \int d(\cos\theta)\epsilon(\theta) = E_{tot.,\gamma}$, where $E_{tot.,\gamma}$ is the total energy in gamma-rays.

²Using the equation $E_{iso}(\theta_v) = E_{iso,0} \cdot y(\theta_v)$

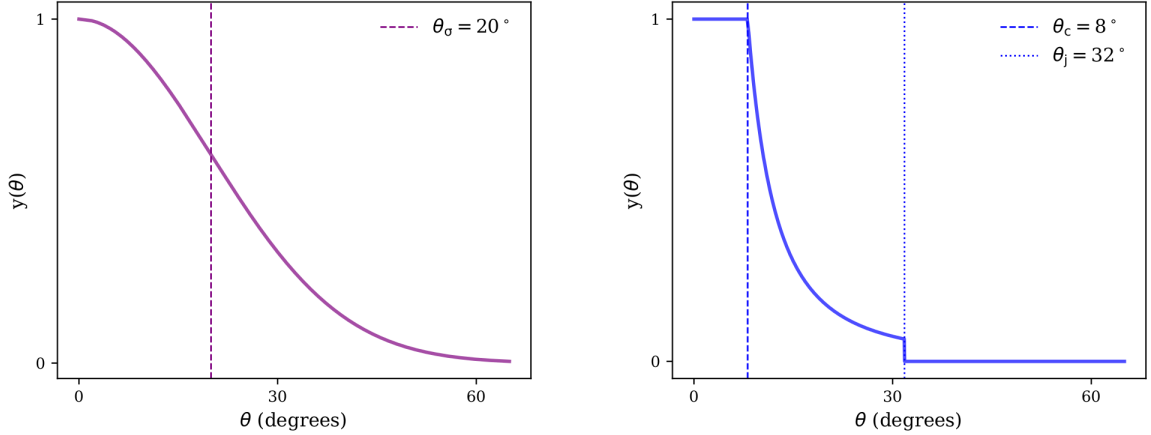


Figure 1.3: Functional forms of the jet structure models, as considered by Hayes et al. 2020. (Left) The gaussian jet structure with a width $\theta_\sigma = 20^\circ$, also marked by the dashed line. (Right) The power-law structure with a core angle $\theta_c = 8^\circ$ and a jet angle $\theta_j = 32^\circ$.

This report deals exclusively with the intrinsic jet structure, and given the functional forms relevant for describing the intrinsic jet structure, the observed jet structure is computed. In order to do this, following Granot et al. 2002, consider the emission profile of a point source moving at some angle with the observer, essentially rendering this scenario off-axis. This geometry will affect the prompt jet emission, as well as the initial afterglow, and thus warrants careful analysis. Now, let the initial jet opening angle be θ_0 and let the observer be at an angle θ_{obs} . In general, for a point source moving at any angle θ with respect to the observer, the observed flux is given by :

$$F_\nu = \frac{L'_{\nu'}}{4\pi d_L^2} \left(\frac{\nu}{\nu'} \right)^3 = \frac{1+z}{4\pi d_L^2} \frac{L'_{\nu'}}{\gamma^3 (1-\beta \cos \theta)^3} \quad (1.3)$$

Here, $L'_{\nu'}$ and ν' are the jet comoving frame spectral luminosity and frequency, d_L is the luminosity distance, $\gamma = (1-\beta^2)^{-1/2}$ is the jet Lorentz factor. If t and ν are the observed time and frequency for an observer at θ , and t_0 and ν_0 are those for an observer on the axis, then:

$$\frac{t_0}{t} = \frac{\nu}{\nu_0} = \frac{(1-\beta)}{(1-\beta \cos \theta)} \equiv a \approx \frac{1}{(1+\gamma^2 \theta^2)} \quad (1.4)$$

And finally putting Eq. 1.4 into Eq. 1.3 and expanding using a Taylor series

approximation upto the leading order:

$$F_\nu(\theta_{obs}, t) = a^3 F_{\nu/a}(0, at) \quad (1.5)$$

This equation can hence be used to relate observed off-axis quantities to the on-axis ones. Furthermore, this enables a transfer from an intrinsic structure to an observed one, which is what was required.

Since in this report, major focus is given to the EM outflows from NSBH mergers, the background presented here about the possible EM outflows from BNS mergers suffices. The interested reader is referred to Ioka and Nakamura 2019, Mohan, Saleem, and Resmi 2019 & Lee and Ramirez-Ruiz 2007 for more detailed discussions on the properties of EM outflows from BNS mergers.

1.2 Outflows from NSBH Mergers

The major difference in the NSBH merger pathway to SGRBs, compared to the case of BNS mergers, is that though there is theoretical and simulational support for the launching of SGRB jets from the merger of a neutron star and a black hole of appropriate mass (see for example Ruiz et al. 2020, Shibata and Hotokezaka 2019, Francois Foucart 2020), there has not been strong observational evidence for the same. In the first half of the third observing run of the LVC (also known as O3a), there have been several triggers which are reportedly confident NSBH triggers. However, there were no counterpart EM signals picked up, which decreases the credibility of NSBH mergers as the progenitors of SGRBs.

The electromagnetic component from NSBH mergers, is largely decided based on the amount of mass left post-merger, outside the horizon of the remnannt black hole. This decides how much matter participates in the subsequent processes, which may be the rapid neutron-capture process which gives rise to the kilonova signal (Metzger 2019) or the magnetic field amplification process via the Magneto-Rotational Instability (MRI) which leads to a SGRB jet (Postnov, Kuranov, and Simkin 2019).

Qualitatively, for a binary where the neutron star is treated as a test mass and the black hole's spin is aligned with the orbital angular momentum of the binary, the innermost-stable circular orbit radius r_{ISCO} scales as $r_{ISCO} \sim f(\chi_{BH})GM_{BH}/c^2$ (where f is a function ranging from 1 to 9, decreasing for increasing (prograde) spins; see Bardeen, Press, and Teukolsky 1972) and the radius at which the tidal disruption

of the neutron star occurs, r_{dis} scales as $r_{dis} \sim k(M_{BH}/M_{BNS})^{1/3}R_{NS}$ (where k is a constant with a dependence on the black hole spin and the equation of state). Only requiring that $r_{dis} \gtrsim r_{ISCO}$, as a rough requirement that disruption should occur before the neutron star plunges into the black hole, leads to the conclusion that for disruption, one requires:

- a.) Low-mass black holes, since $r_{dis} \propto M_{BH}$.
- b.) Larger NS radii, since $r_{dis} \propto M_{NS}^{-1}$. This also implies that the 'softer' equations of state can disfavour tidal disruptions. This is because a softer equation of state will lead to smaller NS radii, and thus not much disruption would occur before the NS plunges into the black hole.
- c.) Higher prograde BH spins, since r_{ISCO} decreases for higher prograde BH spins.

These conclusions can be reached from Fig. 1.4 as well. However, for quantitative results, simulations need to be performed such the effect of the various components in the problem are correctly taken into account (for a summary, see Fig. 1.5). As seen from the literature, where the requisite general-relativistic magnetohydrodynamic simulations are carried out, the matter left over post-merger heavily depends on:

- **The mass ratio of the system.** This is defined as $\mathcal{Q} = M_{BH}/M_{NS}$ so that $\mathcal{Q} > 1$ always. Fully general relativistic, magnetohydrodynamic simulations (such as Ruiz et al. 2020) show that in cases where the mass ratio is 3:1, regardless of the neutron spin, a collimated outflow is observed, whereas the same is not realised in all cases where the mass ratio is 5:1 or higher, and only occurs for high black hole spin cases.
- **The spin of the components of the system.** In geometrized units (where $G = c = 1$), these are prescribed in terms of a_{BH}/M_{BH} or a_{NS}/M_{NS} . Whether these two spins align (prograde) or are anti-aligned (retrograde) decides whether the neutron star would be tidally disrupted (and hence participate in the processes mentioned previously) or not, respectively. Via simulations, it is seen that the more the prograde spin of the neutron star, the farther out it is tidally disrupted, albeit this is only observed for the case of $\mathcal{Q} = 3:1$ (comparing say, Figs. 1.6 and 1.7). Also, this leads to long tidal tails which produces a baryon-loaded environment and thus, the magnetic field of the tidally disrupted matter must overcome the baryon ram pressure to launch the jet. This process hence delays the launching of the jet.

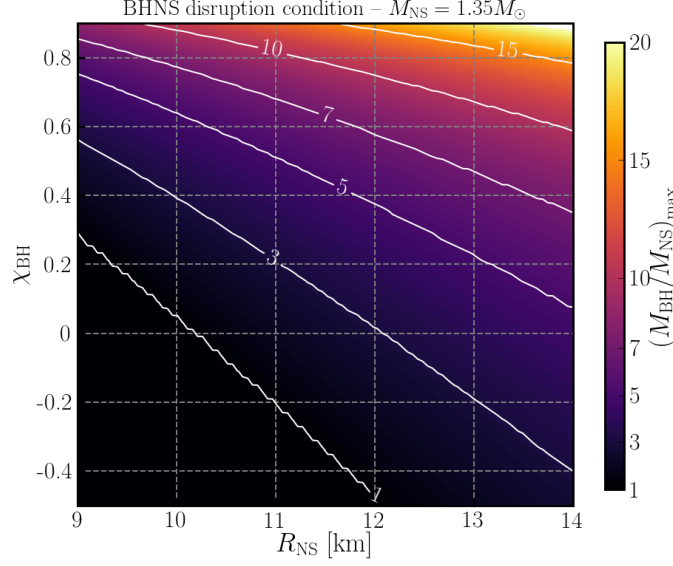


Figure 1.4: Maximum value of the mass-ratio (M_{BH}/M_{NS}) for which a NSBH system disrupts, as a function of the neutron star radius R_{NS} , and the aligned component of the dimensionless black hole spin χ_{BH} , assuming $M_{NS} = 1.35M_{\odot}$. Results for other neutron star masses can be obtained by rescaling considering the disruption condition at constant compaction $C_{NS} = GM_{NS}/R_{NS}c^2$. From Francois Foucart 2020.

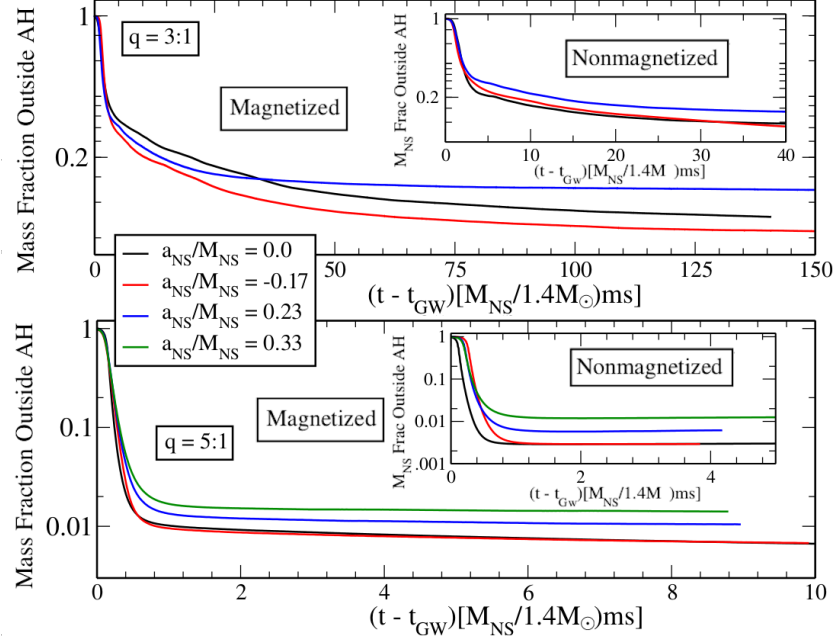


Figure 1.5: Fraction of rest-mass of the NS outside the apparent horizon of the black hole as a function of coordinate time, for the various configurations considered in Ruiz et al. 2020. The inset figures report the same for non-magnetized cases, and the coordinate time is shifted such that the merger time coincides with 0.

Aside from the SGRB jet, which requires magnetic field amplification (via MRI) as well as thermal pair production (from the disk remnant) followed by the Blandford-Znajek process, there is a possibility that NSBH mergers can produce kilonovae signatures (Barbieri, Salafia, Colpi, et al. 2019). For this, the dynamically ejected mass has to be between $10^{-4.5} - 10^{-2}(M_{NS}/1.4M_{\odot})M_{\odot}$ (see Ruiz et al. 2020 for more details), and this will lead to kilonovae potentially detectable by the Large Synoptic Survey Telescope (LSST).

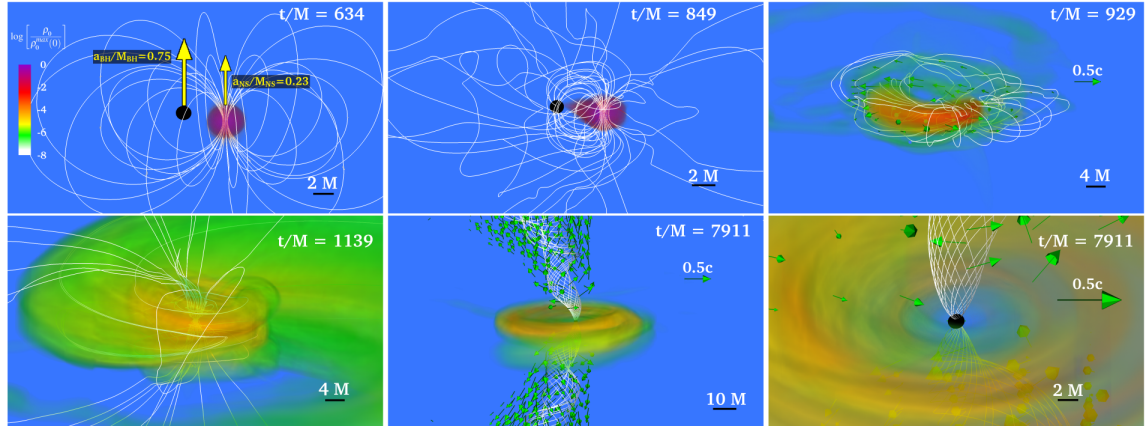


Figure 1.6: Volume rendering of the rest mass density (ρ_0) (in log scale), normalized to the NS maximum value $\rho_0 = 8.92 \times 10^{14}(1.4M_{\odot}/M_{NS})^2$ g/cm³, for particular times for a magnetized neutron star, with $Q = 3:1$ and a prograde NS spin of 0.23. Top three panels highlight the inspiral and tidal disruption, whereas the bottom three panels highlight the appearance of the magnetically-driven jet. White lines denote the magnetic field, arrows denote the fluid velocity and the BH's apparent horizon is the black sphere. Here $M = 2.5 \times 10^{-2}(M_{NS}/M_{1.4M_{\odot}})$ ms = $7.58(M_{NS}/M_{1.4M_{\odot}})$ km (in geometrized units). From Ruiz et al. 2020.

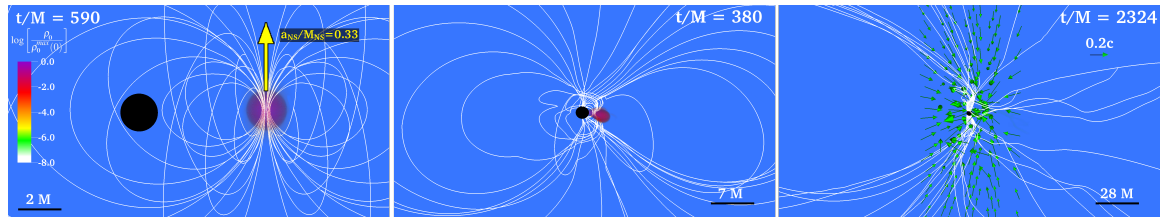


Figure 1.7: Similar to Fig. 1.6, however with the NS spin being 0.33, the BH spin being 0 and $q = 5:1$. In this case, no strong collimation of the magnetic field is observed from the merger remnant, and so a magnetically-driven jet is also not observed. From Ruiz et al. 2020.

1.2.1 Modelling outflows from NSBH Mergers

As mentioned before, the outflows from NSBH mergers depend on the amount of mass left outside the event horizon post-merger. In the work done by Francois Foucart, Hinderer, and Nissanke 2018, the authors consider a suite of 75 numerical relativity simulations of NSBH mergers over the parameter space $\mathcal{Q} \in [1, 7]$, $\chi_{BH} \in [-0.5, 0.97]$, $C_{NS} \in [0.13, 0.182]^3$ and fit the results for the *remnant mass* M_{rem} (sometimes also denoted as M_{out}), as a function of the binary parameters (masses, spins of the components, tidal deformability of the neutron star etc). This fit is given as follows:

$$M_{\text{out}} = M_{NS}^b \cdot \max \left(\alpha \frac{1 - 2\rho}{\eta^{1/3}} - \beta \hat{R}_{\text{ISCO}} \frac{\rho}{\eta} + \gamma, 0 \right)^\delta \quad (1.6)$$

where:

- The baryonic mass of the neutron star is given by the equation

$$M_{NS}^b = M_{NS} \left(1 + \frac{0.6C_{NS}}{1 + 0.5C_{NS}} \right)$$

- The tidal deformability of the neutron star is given by Λ_{NS} and $\rho = (15\Lambda_{NS})^{-1/5}$. It is also related to the compactness of the neutron star via the C–Love relation (see Yagi and Yunes 2017):

$$C_{NS} = \sum_{k=0}^2 a_k (\ln \Lambda_{NS})^k \quad (1.7)$$

where $a_0 = 0.360$, $a_1 = -0.0335$, $a_2 = 0.000705$.

- η is the symmetric mass ratio, given by $\eta = \frac{\mathcal{Q}}{(1 + \mathcal{Q})^2}$.
- $\hat{R}_{\text{ISCO}} = c^2 R_{\text{ISCO}} / GM_{BH}$ is the normalized ISCO radius for a spinning black hole, given in Bardeen, Press, and Teukolsky 1972 as :

$$\begin{aligned} \hat{R}_{\text{ISCO}} &= 3 + Z_2 - \text{sgn}(\chi_{BH}) \sqrt{(3 - Z_1)(3 + Z_1 + 2Z_2)} \\ &\hookrightarrow Z_1 = 1 + (1 - \chi_{BH}^2)^{1/3} [(1 + \chi_{BH})^{1/3} + (1 - \chi_{BH})^{1/3}] \\ &\hookrightarrow Z_2 = \sqrt{3\chi_{BH}^2 + Z_1^2} \end{aligned} \quad (1.8)$$

³Here, $\mathcal{Q} = M_{BH}/M_{NS}$ is the mass-ratio, $\chi_{BH} = c|\mathbf{S}|/GM_{BH}^2$ is the effective spin of the black hole and $C_{NS} = GM_{NS}/R_{NS}c^2$ is the compactness of the neutron star.

- $(\alpha, \beta, \gamma, \delta) \equiv (0.308, 0.124, 0.283, 1.536)$ are the fit coefficients.

Similarly, Kawaguchi et al. 2016 fit to the results of 45 numerical relativity simulations over the parameter space $\mathcal{Q} \in [3, 7]$, $\chi_{\text{BH}} \in [0, 0.90]$, $C_{\text{NS}} \in [0.138, 0.180]$. This fit produces a formula for the *dynamic* mass M_{dyn} , which is the unbound mass ejected at the time of disruption, in terms of the binary parameters. This fit is given as follows:

$$\frac{M_{\text{dyn}}}{M_{\text{NS}}^b} = \max \left\{ a_1 Q^{n_1} (1 - 2C_{\text{NS}}) C_{\text{NS}}^{-1} - a_2 Q^{n_2} \hat{R}_{\text{ISCO}}(\chi_{\text{BH}}) + a_3 \left(1 - \frac{M_{\text{NS}}}{M_{\text{NS}}^b} \right) + a_4, 0 \right\} \quad (1.9)$$

where the symbols have their usual meanings, and additionally:

$$\begin{aligned} a_1 &= 4.464 \times 10^{-2} & a_2 &= 2.269 \times 10^{-3} \\ a_3 &= 2.431 & a_4 &= -0.4159 \\ n_1 &= 0.2497 & n_2 &= 1.352 \end{aligned}$$

From these two quantities, one can derive the disc mass M_{disc} as :

$$M_{\text{disc}} = \max\{M_{\text{out}} - M_{\text{dyn}}, 0\} \quad (1.10)$$

However, due to the fact that these two fits are derived from simulations over different regions of the input parameter space, care must be taken while applying them together. This is to ensure that $M_{\text{dyn}} \leq M_{\text{out}}$ always, so that the disc mass is non-negative. This validation is performed by considering the ratio $M_{\text{out}}/M_{\text{dyn}}$. Another constraint is imposed, which is motivated by the fact that NSBH simulations carried out by F. Foucart et al. 2019 in the near-equal mass ratio regime found an unbound component no more massive than roughly 30% of the total remnant mass (note that one expects maximal tidal disruption in this regime, given a fast spinning black hole). Thus we set:

$$M_{\text{dyn,max}} = f \cdot M_{\text{rem}} = 0.3 \cdot M_{\text{rem}} \quad (1.11)$$

Additionally, the masses of the other wind ejecta, namely the neutrino-driven and

viscosity-driven wind ejecta, are derived from that of the disc mass:

$$\begin{aligned} M_{\text{vis}} &= \xi_{\text{vis}} M_{\text{disc}} = 0.2 M_{\text{disc}} \\ M_{\nu} &= \xi_{\nu} M_{\text{disc}} = 0.01 M_{\text{disc}} \end{aligned} \quad (1.12)$$

To model the SGRB jet, the procedure of Zhu et al. 2020 is followed. The kinetic energy of the jet is decided by the disc mass and the black hole spin as follows:

$$E_{\text{K,jet}} = \epsilon(1 - \xi_{\text{vis}} - \xi_{\nu})M_{\text{disc}}c^2\Omega_H^2f(\Omega_H) \quad (1.13)$$

where:

- The dimensionless angular velocity at the horizon of the black hole is given by:

$$\Omega_H = \frac{\chi_{BH}}{2(1 + \sqrt{1 + \chi_{BH}^2})} \quad (1.14)$$

- $f(\Omega_H)$ is a high-spin correction factor given by:

$$f(\Omega_H) = 1 + 1.38\Omega_H^2 - 9.2\Omega_H^4 \quad (1.15)$$

- ϵ is a fudge factor which depends on the large-scale geometry of the magnetic field, disc aspect ratio and the ratio of the magnetic field energy density to disc pressure at saturation.

In order to set it to a definite value, it is noted that the maximum disc mass cannot exceed the total NS baryonic mass i.e. $M_{\text{disc}} \lesssim 2M_{\odot}$. Also, the spin-dependent factor $\Omega_H^2f(\Omega_H)$ cannot exceed 0.2 (since $\chi_{BH} \in [-1, 1]$). Furthermore, the most energetic of SGRBs has had a $E_{\gamma,\text{iso}} \sim 7.4 \times 10^{52}$ erg, and if one assumes a 10% conversion efficiency of kinetic to gamma-ray energy along-with a typical jet opening angle of 5° , this corresponds to a kinetic energy of $E_{\text{K,jet}} \sim 3 \times 10^{52}$ erg.

Based on this, one can calculate $\boxed{\epsilon \approx 0.015}$.

However, note that in Eq. 1.14, the value of χ_{BH} is the *spin of the remnant BH*,

which can be computed solving the following implicit equation (Pannarale 2013):

$$\chi_{BH,f} = \frac{\chi_{BH,i} M_{BH}^2 + l_z(\hat{R}_{ISCO,f}, \chi_{BH,f}) M_{BH} [(1 - f(\eta)) M_{NS} + f(\eta) M_{b,NS} - M_{out}]}{[M(1 - (1 - e(\hat{R}_{ISCO,i}, \chi_{BH,i}))\eta) - e(\hat{R}_{ISCO,i}, \chi_{BH,i}) M_{out}]} \quad (1.16)$$

for $\chi_{BH,f}$, where:

- $\chi_{BH,i}$ and $\chi_{BH,f}$ are the initial and final spins of the BH and BH remnant respectively.
- M_{BH} and M_{NS} are the masses of the BH and NS respectively. $M_{b,NS}$ and M_{out} are the baryonic mass of the NS and the remnant mass for the particular NSBH merger calculated using Eq. 1.6 respectively. Finally, M is the total (initial) mass of the binary, and $\eta = \frac{Q}{(1+Q)^2}$ is the initial symmetric mass ratio. All mass quantities are expressed in geometrized units, i.e. where $G = c = 1$.
- $l_z(\hat{R}_{ISCO,f}, \chi_{BH,f})$ is the orbital angular momentum per unit mass of a test particle orbiting the remnant BH at the ISCO. Note that here \hat{R}_{ISCO} plays the role of the (dimensionless) radial Boyer-Lindquist coordinate, useful for describing the orbits in the Kerr spacetime around this rotating BH remnant. Additionally, $\hat{R}_{ISCO,f}$ refers to the value computed by using the final BH spin in Eq. 1.8. Also for a given radial coordinate, \hat{R} and a BH spin, χ this orbital angular momentum is given as:

$$l_z(\hat{R}, \chi) = \text{sgn}(\chi) \left[\frac{\hat{R}^2 - \text{sgn}(\chi) \cdot 2\chi\sqrt{\hat{R}} + \chi^2}{\sqrt{\hat{R}}(\hat{R}^2 - 3\hat{R} + \text{sgn}(\chi) \cdot 2\chi\sqrt{\hat{R}})^{1/2}} \right] \quad (1.17)$$

where $\text{sgn}(\chi)$ is positive/negative for prograde/retrograde orbits.

- $e(\hat{R}_{ISCO}, \chi_{BH,f})$ is the energy per unit mass of a test particle orbiting the remnant BH at the ISCO. For equatorial Kerr orbits at a radial coordinate, \hat{R} around a BH with a spin, χ it is given as:

$$e_z(\hat{R}, \chi) = \frac{\hat{R}^2 - 2\hat{R} + \text{sgn}(\chi) \cdot \chi\sqrt{\hat{R}}}{\hat{R}(\hat{R}^2 - 3\hat{R} + \text{sgn}(\chi) \cdot 2\chi\sqrt{\hat{R}})^{1/2}} \quad (1.18)$$

- $f(\eta)$ is a transition function to smooth the behaviour of this equation in the transition from large ($Q \geq 4$) mass ratio mergers to smaller ($Q \in (2, 4]$) mass

ratio mergers. This function is not uniquely defined, but Pannarale 2013 defines it using the following properties which are validated by comparing with numerical relativity simulations:

- $f(\eta \geq 2/9) = 1$ and $f(\eta \leq 0.16) = 0$. This means that for mergers with relatively large mass ratios ($\mathcal{Q} \geq 4 \Leftrightarrow \eta \leq 0.16$) the function ‘switches off’ and for lower mass ratios ($\mathcal{Q} \leq 2 \Leftrightarrow \eta \geq 2/9$) the function ‘switches on’.
- $\frac{df}{d\eta} \geq 0 \quad \forall \eta \in (0, 0.25] \Leftrightarrow \mathcal{Q} \in (1, \infty)$. This means that the transition function is monotonically increasing. Additionally for simplicity, it is assumed to be C^∞ .

With these constraints in mind, the transition function is defined as:

$$f(\eta) = \begin{cases} 0, & \eta \leq 0.16 \\ \frac{1}{2} \left[1 - \cos \left(\frac{\pi(\eta - 0.16)}{2/9 - 0.16} \right) \right], & 0.16 < \eta < 2/9 \\ 1, & 2/9 \leq \eta \leq 0.25 \end{cases} \quad (1.19)$$

Now, given the jet energetics using the equations above, one can define the structure of the SGRB jet, given by the following equations:

$$\frac{dE(\theta)}{d\Omega} = \frac{E_{k,jet}}{\pi\theta_{c,E}^2} e^{-(\theta/\theta_{c,E})^2} \quad (1.20)$$

$$\Gamma(\theta) = (\Gamma_c - 1)e^{-(\theta/\theta_{c,E})^2} + 1 \quad (1.21)$$

$$E_{iso}(\theta_v) = \eta \int \frac{\delta^3 dE}{\Gamma d\Omega} d\Omega \quad (1.22)$$

where:

- $\Gamma_c = 100, \theta_{c,E} = 0.1, \theta_{c,\Gamma} = 0.2$. See Salafia et al. 2015 and Barbieri, Salafia, Perego, et al. 2019.
- η is the conversion efficiency of gamma-ray energy to kinetic energy, which is traditionally taken to be 10%.

- δ is the Doppler factor, given by

$$\delta = \frac{1}{\Gamma[1 - \beta \cos \alpha_v]}$$

where α_v is the angle between the jet element at (θ, ϕ) and the observer's direction.

1.3 NS mergers in GW regime

Consider any astrophysical source emitting gravitational waves, which come in two polarizations, namely the *plus* $h_+(t; \Theta_{GW})$ and the *cross* $h_\times(t; \Theta_{GW})$ polarizations. Here Θ_{GW} is the parameter vector, typically taken to be $\{m_1, m_2, \chi_1, \chi_2, D_L, \iota, t_c, \phi_c\}$ which are the component masses, component spins, the binary's luminosity distance, the inclination angle of the orbital plane with respect to the line of sight, and two constants of integration: the time and phase of coalescence, respectively.

A detector's response is recorded as the GW strain such waves produce, but in the frequency domain and so the input signals are Fourier transformed before processing. Also the detector's antenna patterns (sensitivity as a function of the source location on the sky) and location phase factor (effect of the earth's rotation) play a role in the response. Thus, the detector response to these gravitational waves is of the form:

$$H(f; \Theta) = F_{lp}(f; \alpha, \delta) \cdot [H_+(f; \Theta_{GW})F_+(f; \alpha, \delta, \psi) + H_\times(f; \Theta_{GW})F_\times(f; \alpha, \delta, \psi)] \quad (1.23)$$

where F_{lp} is the location phase factor as a function of the frequency and the source right-ascension and declination, $H_{+/\times}$ are the frequency domain waveforms, and $F_{+/\times}$ are the detector antenna patterns for each polarization. Also $\Theta = \{\Theta_{GW}, \alpha, \delta, \psi\}$. The sensitivity of a detector is given by the detector's noise $n(t)$ and its autocorrelation $\kappa = \overline{n(t_1)n(t_2)}$. Usually, the noise is assumed to be stationary, zero-mean and Gaussian. Thus, one can define the one-sided power spectral density $S_n(f)$ as the Fourier transform of the autocorrelation.

From this, one can define the ‘overlap’ between two GW signals (for eg.: the detector responses for two different waveforms) using the noise-weighted scalar product:

$$\langle H, G \rangle = 2 \int_0^\infty \frac{H(f)G^*(f) + H^*(f)G(f)}{S_n(f)} df \quad (1.24)$$

And using this definition of the scalar product, the signal-to-noise ratio is defined as:

$$\rho^2 = \langle H, H \rangle = 4 \int_0^\infty \frac{|H(f)|^2}{S_n(f)} df \quad (1.25)$$

Now, since the noise $n(t) = s(t) - h(t)$ is assumed to a zero-mean Gaussian, its Fourier transform also behaves the same way, and thus the probability of noise can be written down as :

$$p(\Theta) = p^0(\Theta) e^{-\frac{1}{2} \langle S - H(\Theta), S - H(\Theta) \rangle} \quad (1.26)$$

where p^0 is the prior on the parameter vector of the detector response. Assuming that an event signal S has a high SNR, the value of Θ at peak probability is a good estimate of the true value Θ^* . Additionally peak probability occurs when the exponential $E = \langle S - H, S - H \rangle$ is the largest. Expanding it around the maximum value:

$$E(\Theta) = E(\Theta^*) + \frac{1}{2} \frac{\partial^2 E(\Theta)}{\partial \Theta_i \partial \Theta_j} \Big|_{\Theta=\Theta^*} \Delta \Theta_i \Delta \Theta_j + \dots \quad (1.27)$$

where $\Delta \Theta_i = \Theta_i - \Theta_i^*$. The Hessian given by:

$$\frac{\partial^2 E(\Theta)}{\partial \Theta_i \partial \Theta_j} = 2 \langle \partial_{\Theta_i} H(\Theta), \partial_{\Theta_j} H(\Theta) \rangle + \langle \partial_{\Theta_i} \partial_{\Theta_j} H(\Theta), N \rangle \quad (1.28)$$

can be simplified for large SNR, where second-order differentials become negligible. This leads to the definition of the Fisher Information Matrix Γ :

$$\Gamma_{ij} = \langle \partial_{\Theta_i} H(\Theta), \partial_{\Theta_j} H(\Theta) \rangle \quad (1.29)$$

And hence, Eqn. 1.26 becomes:

$$p(\Theta) \sim \exp \left(-\frac{1}{2} \Gamma_{ij} \Delta \Theta_i \Delta \Theta_j \right) \quad (1.30)$$

which implies that the assumption of Gaussian noise helps associate the FIM to the inverse of the covariance matrix $\Sigma \equiv \Gamma^{-1}$. This also means that the diagonal and off-diagonal elements of Γ^{-1} denote the variances and covariances of the parameters, respectively, with 1σ estimates of the error are given as $\sigma_{\Theta_i} = \sqrt{\Sigma_{ii}}$.

This Fisher Information Matrix (FIM) formalism is a method of rapid GW data analysis, which approaches the accuracy of traditional Bayesian parameter estimation for

events with large SNR. Sometimes this method is also referred to as the Fisher Information Formalism (FIF), in which case the Fisher information is not a matrix but is instead the variance of the partial derivative with respect to the parameter vector, of the natural logarithm of the likelihood function for the random variable whose parameters are to be estimated.

Software tools such as **GWBENCH** (see Borhanian 2020), leverage this formalism to compute the Fisher matrix for a particular NS merger, given the network configuration and binary parameters. In this way, it enables rapid calculations to benchmark detector upgrades as well as forecast the confidence with which parameters may be estimated for the NS mergers in question.

1.4 Summary

NS mergers can present an ideal testing environment for physical theories under extreme gravity, and by observing them in both the EM and GW windows, current theories can be better understood and refined. Several questions also remain about the exact mechanisms which power the outflows from these NS mergers.

In this report, the focus is mainly on SGRB jets from NSBH mergers and in pursuit of the same, population synthesis studies are carried out to infer the conditions for and implications of observing a SGRB jet from NSBH mergers.

Chapter 2

Population Synthesis

In order to derive meaningful conclusions about the outflows from NS mergers, given the models described in Chapter 1, it was necessary to carry out population synthesis studies. In these studies, population models which are physically or observationally motivated are taken from the literature and used to compute the statistical properties of outflows from NS binaries synthesized from these models. If no confident or relevant model was yet described in literature, physically motivated ansätze are used (see for example, §§2.1.2).

In each study which uses (slightly) different population models, 10^5 samples were drawn from the relevant parameter distributions. Using these as inputs, the expected outflows were calculated using the fit formulae described in Chapter 1 for the outflows from NSBH mergers.

In this chapter, the various population models are briefly described along with their pertinence. Furthermore, preliminary checks for the population synthesis code are also discussed, which help verify the consistency of the code with theoretical results.

2.1 Black Hole Population Models

2.1.1 Mass, M_{BH}

The masses of the black holes was sampled from the TRUNCATED mass distribution from The LIGO Scientific Collaboration et al. 2020. The distribution ‘produces’ black holes with masses between $3\text{--}100 M_\odot$ (as can be seen from Fig. 2.2). However, NS binaries with extremely massive ($M_{BH} > 20M_\odot$) black holes will not produce any appreciable EM emission, due to the NS companion plunging into the black hole directly. For this reason, an upper limit of $20 M_\odot$ is imposed on the black hole masses

sampled in the population synthesis code.

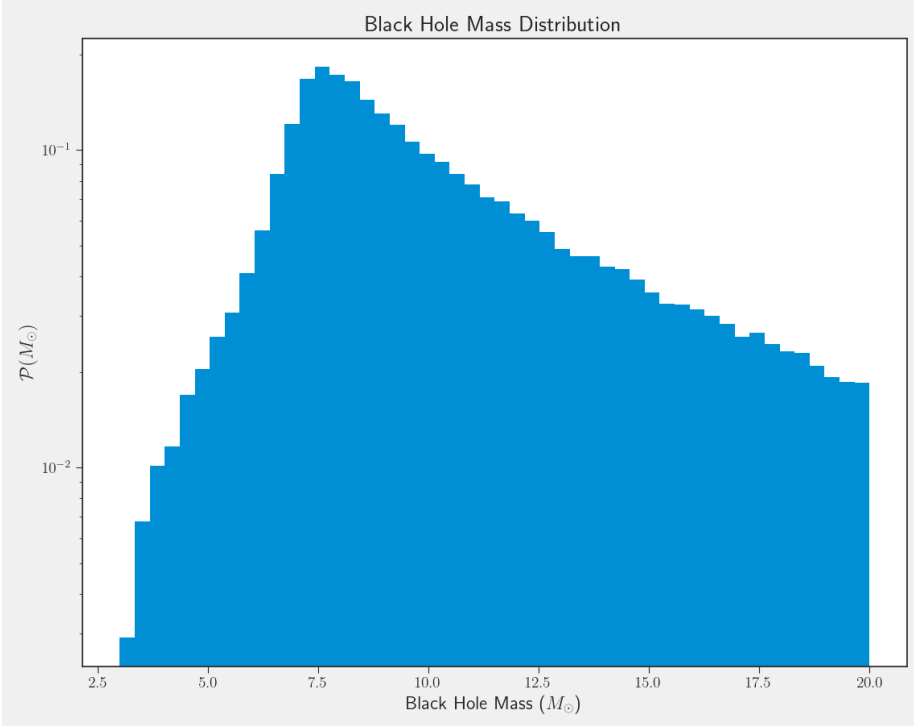


Figure 2.1: Black hole mass distribution as used in the current report, with an upper limit of $20 M_{\odot}$.

2.1.2 Spin, χ_{BH}

The spins of the black holes are sampled from the DEFAULT distribution given in The LIGO Scientific Collaboration et al. 2020. This distribution is essentially a Beta distribution, which ensures that the spin parameters sampled from this distribution remain within $[0, 1]$.

However, since there have been not many confident NSBH merger detections in the GW regime, this distribution is largely derived from observing BBH mergers, and thus may not represent the true spin distribution of black holes in NSBH binaries. To circumvent this, the following ansätze are used to probe the effect of the spin distribution on the EM outflows:

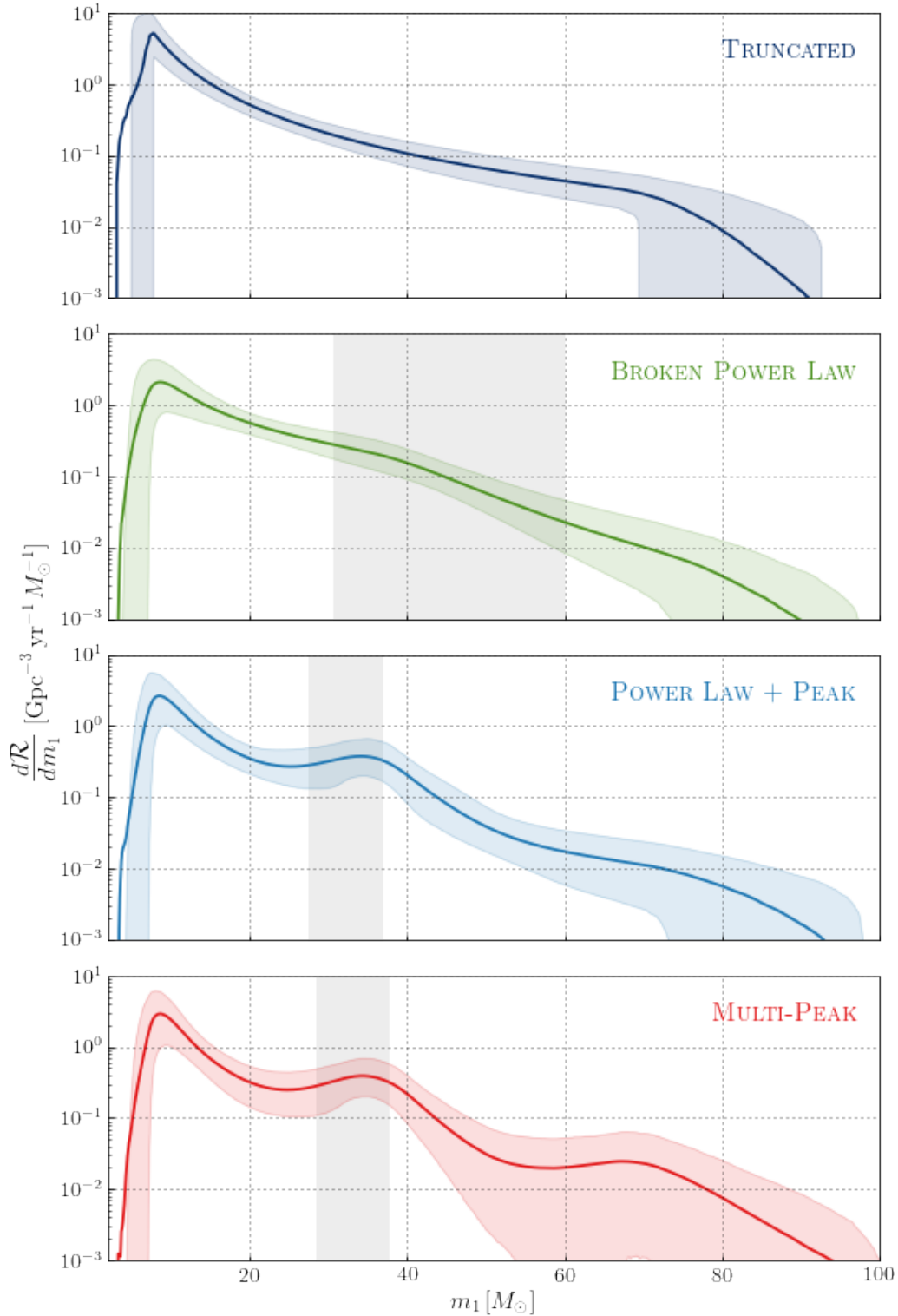


Figure 2.2: Black Hole Mass Distributions from The LIGO Scientific Collaboration et al. 2020. In the current study, the TRUNCATED mass distribution with an upper limit at $20 M_\odot$, since more massive black holes would not produce significant EM emission when in a merging NSBH binary.

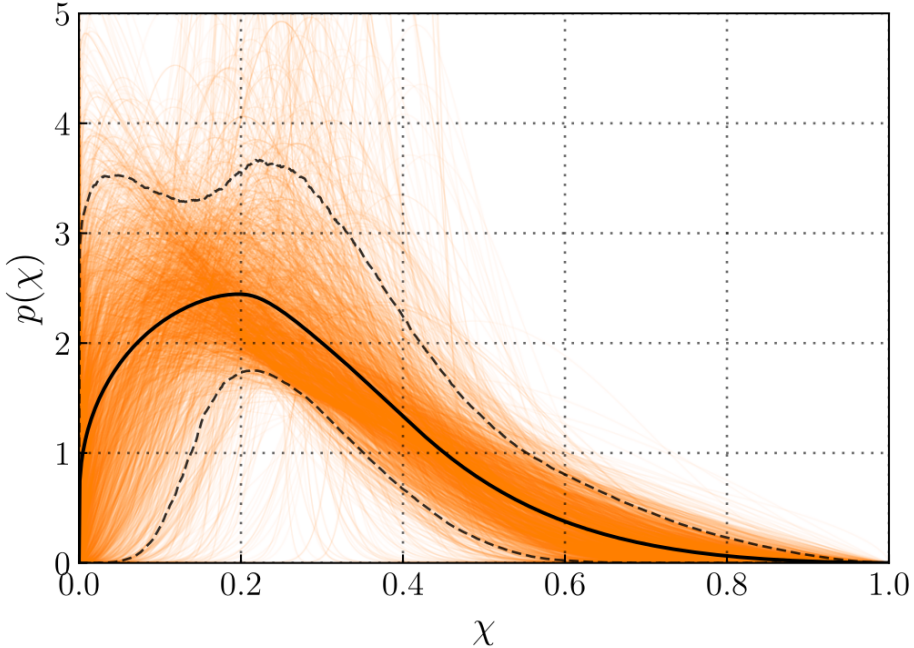


Figure 2.3: Beta distribution for the black hole spin from The LIGO Scientific Collaboration et al. 2020. Here the light traces are samples from the posterior distribution, whereas the solid black line is the posterior probability distribution for χ_{BH} . Dashed black lines mark the 90% quantiles for the same.

- Uniform spin distribution: here $\chi_{BH} \sim \mathcal{U}(0, 1)$. Note also that this distribution will have a *higher number of high spin samples* as compared to the DEFAULT distribution considered above.

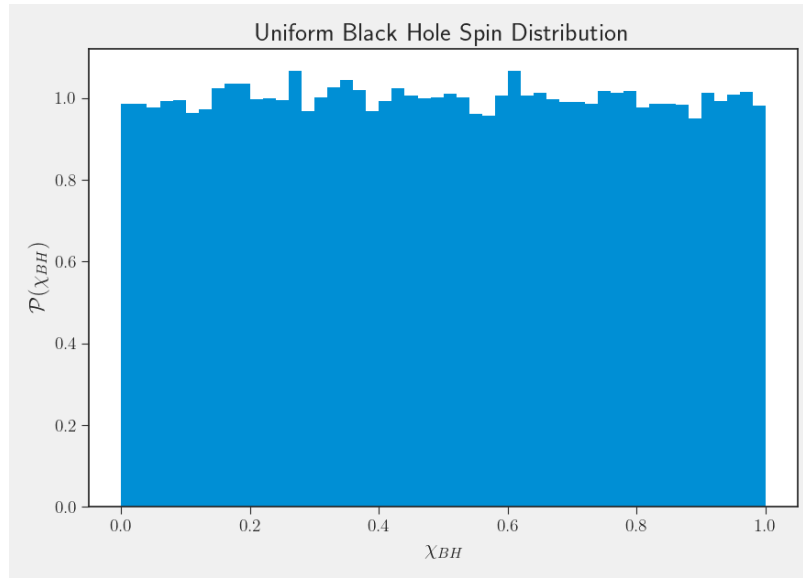


Figure 2.4: A realisation of the uniform black hole spin distribution considered here.

- Gaussian spin distributions: here $\chi_{BH} \sim \mathcal{N}(\mu, \sigma)$, but samples outside of $[0, 1]$ are not considered. Here, μ, σ represent the mean and standard deviation, respectively, of the Gaussian distribution. For simplicity and to cover a representative number out of all the possible distributions, samples were taken from $\mathcal{N}(0.2, 0.2)$, $\mathcal{N}(0.5, 0.2)$ and $\mathcal{N}(0.7, 0.2)$. These represent distributions concentrated around low, medium and high spins respectively.

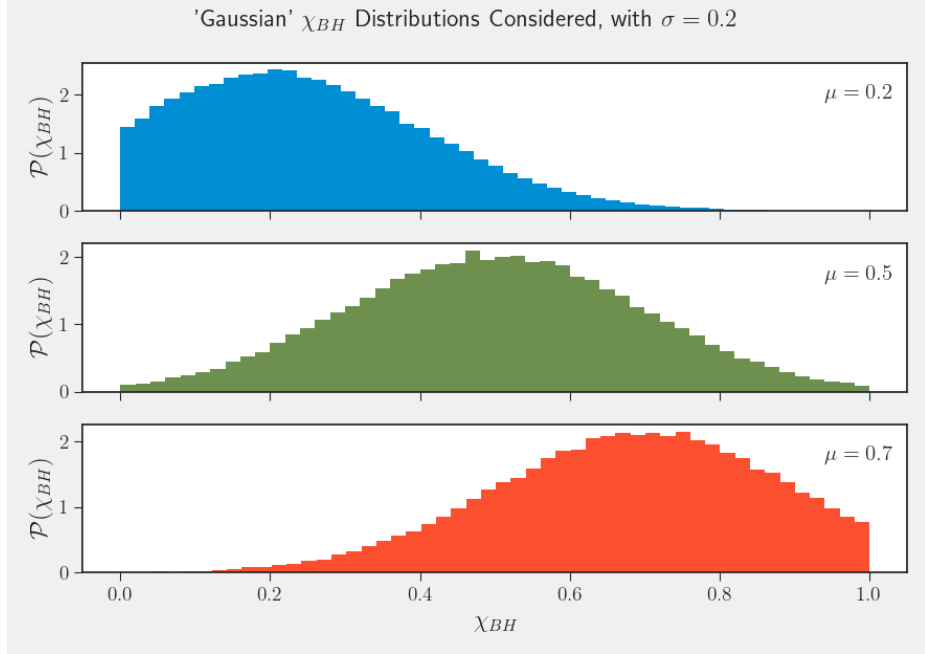


Figure 2.5: Realisations of the various ‘Gaussian’ black hole spin distributions considered here.

2.2 Neutron Star Population Models

In order to reduce the number of variables in the problem, the masses and radii of all neutron stars in the population was set to $1.4 M_\odot$ and 11 km respectively. These values correspond to the median values inferred for GW170817 (see B. P. Abbott et al. 2018). Also, the spins of all neutron stars synthesized was set to 0, since it is assumed that sufficient amount of time would have passed between the formation of the binary and merger, allowing for the neutron star to spin down such that $\chi_{NS} \sim 0$. Additionally, the tidal deformability of the neutron stars, Λ_{NS} was set using the C-love relation (see Yagi and Yunes 2017). In order to do this, the compactness of the

neutron stars, C_{NS} was computed using the relation :

$$C_{NS} = \frac{GM_{NS}}{R_{NS}c^2} \quad (2.1)$$

where M_{NS} , R_{NS} are the mass and radius of the neutron star, G is the universal gravitational constant and c is the speed of light. Finally, the tidal deformability is computed by solving the C-Love relation :

$$C_{NS} = \sum_{k=0}^2 a_k (\ln \Lambda_{NS})^k \quad (2.2)$$

where Λ_{NS} is the tidal deformability of the neutron star, and a_k are the fit coefficients as given in Yagi and Yunes 2017.

2.3 Spatial Distribution and Orientation of Samples

2.3.1 Constant comoving volume distribution

The simulated events whose component mass and spin distributions were described in §2.1–2.2 are distributed in 3D space such that their number density is constant in comoving volume.

For this, firstly the latitudinal (θ) and longitudinal (ϕ) angles are sampled such that $\cos \theta \sim \mathcal{U}(-1, 1)$ and $\phi \in \mathcal{U}(0, 2\pi)$, i.e. such that they are uniform on a unit sphere. As for the comoving distance distribution $\mathcal{P}(D_c)$, consider the probability of an event lying in an infinitesimal shell of width dD_c at a comoving distance D_c . Then it can be seen that:

$$\mathcal{P}(D_c)dD_c \propto D_c^2 dD_c \Rightarrow \boxed{\mathcal{P}(D_c) = \alpha D_c^2} \quad (2.3)$$

where α is the constant of proportionality. In the local universe, it can be safely assumed that $D_c \approx D_L$, where the latter is the luminosity distance. However from the fact that the GW network SNR $\rho \propto D_L^{-1}$, it can also be seen that:

$$\begin{aligned}
\mathcal{P}(\rho) &= \mathcal{P}(D_L) \left| \frac{dD_L}{d\rho} \right| \\
&= \mathcal{P}(D_c) \left| \frac{dD_c}{d\rho} \right| \\
&\propto \frac{1}{\rho^2} \frac{1}{\rho^2} = \frac{1}{\rho^4} \\
\Rightarrow \mathcal{P}(\rho) &= \frac{\beta}{\rho^4}
\end{aligned} \tag{2.4}$$

Once the SNR detection threshold¹ (ρ_{th}) is set, the normalization constants can be computed as follows:

$$\int_0^{D_{c,max}} \mathcal{P}(D_c) dD_c = \int_0^{D_{L,max}} \mathcal{P}(D_L) dD_L \tag{2.5}$$

$$= \int_{\infty}^{\rho_{th}} \mathcal{P}(\rho) d\rho \tag{2.6}$$

$$= 1 \tag{2.7}$$

This gives:

$$\mathcal{P}(D_L) = 3 \frac{D_L^2}{D_{L,max}} \Leftrightarrow \mathcal{P}(\rho) = 3 \frac{\rho_{th}^3}{\rho^4} \tag{2.8}$$

where $D_{L,max}$ is the luminosity distance corresponding to the detection threshold. As an example, for the Advanced LIGO/VIRGO design configuration and a network SNR threshold of 10, $D_{L,max} \approx 1123$ Mpc.

Using Eq. 2.8, samples are drawn from the luminosity distance distribution and using the previous samples for θ and ϕ , events are distributed in 3D space such that the number density of events is constant in the comoving volume.

2.3.2 Orientation of Events

The orientation of NSBH binaries with respect to the line-of-sight is prescribed using the inclination angle, ι and the polarization angle of the incoming GW signal, ψ .

¹This is defined such that any event with a GW network SNR greater than the detection threshold will be considered a detection.

These are distributed in the population synthesis such that $\cos \iota \sim \mathcal{U}(-1, 1)$ and $\psi \sim \mathcal{U}(0, 2\pi)$, from which samples are drawn for individual events.

2.4 Validation of Population Synthesis Code

With the population models for the binary component parameters as described in the previous sections, 10^5 samples are drawn from each model to generate a population. These populations will majorly differ in the black hole spin distribution and are thus distinguished by that very factor.

Given these populations, several checks were carried out to confirm the consistency of the underlying models and the population generated, with the use of (both EM and GW) theoretical results. The rationale behind these checks and the results are given in the following sections.

2.4.1 GW Checks

Firstly, for the samples generated, the optimal GW SNR corresponding to the binary parameter combinations was computed. This was done by using the restricted post-Newtonian (PN) waveform (RWF; see Cutler and Flanagan 1994) as the GW template for the expected strain signal corresponding to an actual merger event. For this case, the template is given using the frequency domain representation:

$$\tilde{h}(f) = \mathcal{A} f^{-7/6} e^{i\phi(f)} \quad (2.9)$$

where $\mathcal{A} = \sqrt{5/96}\pi^{-2/3}\mathcal{M}$ is the amplitude, $\mathcal{M} = M\eta^{5/3}$ is the chirp mass, M is the total mass, $\eta = \frac{m_1 m_2}{M}$ is the symmetric mass ratio, and $\phi(f)$ is the frequency domain GW phase function. With the RWF template, the PN approximations made ensure maximum accuracy with respect to the phase but ignore the PN corrections to the amplitude of the gravitational waveform. However, this tradeoff is beneficial since accurately tracking the phase evolution is vital for inferring the binary masses (Poisson and Will 1995), which helps in classifying which type of compact binary coalescence (CBC) the incoming signal corresponds to. For such a template, the optimal SNR at a detector with a noise power spectral density (PSD) $S_h(f)$, is computed as:

$$\rho = \sqrt{4 \int_0^\infty \frac{|\tilde{h}(f)|^2}{S_h(f)} df} \quad (2.10)$$

Substituting the form of $\tilde{h}(f)$ from Eq. 2.9, one obtains:

$$\rho(m_1, m_2, D_L, \theta, \phi, \psi, \iota) = \left\{ 4 \frac{\mathcal{A}^2}{D_L^2} \left[F_+^2(\theta, \phi, \psi)(1 + \cos^2 \iota)^2 + 4F_x^2(\theta, \phi, \psi) \cos^2 \iota \right] I(M) \right\}^{1/2} \quad (2.11)$$

where $F_{+,x}(\theta, \phi, \psi)$ are the antenna pattern functions for the ‘plus’ and ‘cross’ GW polarizations, and the four angles $\{\theta, \phi, \psi, \iota\}$ prescribe the location and orientation of the source with respect to the detector. Also, $I(M)$ is the frequency integral given by:

$$I(M) = \int_0^\infty \frac{f^{-7/3}}{S_h(f)} df \quad (2.12)$$

$$\approx \int_{f_{low}}^{f_{LSO}} \frac{f^{-7/3}}{S_h(f)} df \quad (2.13)$$

where f_{low} corresponds to the seismic cutoff in the detector noise PSD curve, and f_{LSO} corresponds to the frequency at the last stable orbit for a black hole of total mass M , which under the PN approximation is $f_{LSO} = (6^{3/2}\pi M)^{-1}$.

For each sample in the various populations, the optimal SNR was computed using the above formulae with the aid of the PyCBC (Nitz et al. 2021) Python package along with the LALSimulation C libraries (LIGO Scientific Collaboration 2018a). Using the computed SNRs, it was verified that the events *are* distributed in luminosity distance (and thus SNR) as expected from 2.8. This is given in Fig. 2.6. Note that in order to verify this relation, one must only consider the events whose network SNR is above the threshold SNR chosen (in this case, 10).

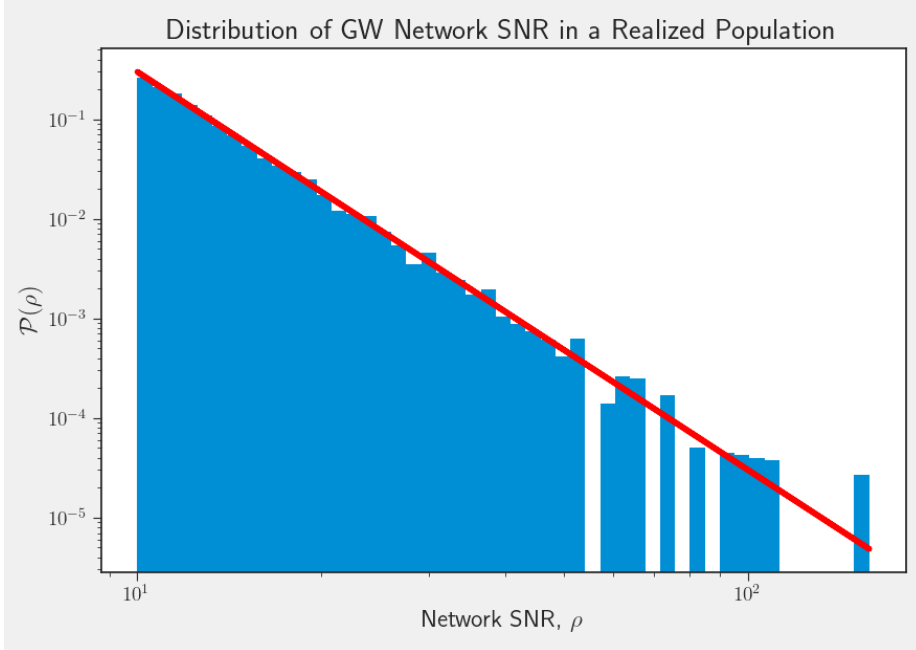


Figure 2.6: Distribution of GW network SNR, from a particular realisation of a population with standard assumptions about binary parameters, and a uniform spin distribution. The red line is the curve given by theoretical considerations, which for a threshold SNR of 10, corresponds to $f(\rho) = 3\rho_{th}^3/\rho^4 = 3000/\rho^4$.

Furthermore, from Eq. 2.11, the GW network SNR is higher in value if:

- The merger ‘event’ is closer by, i.e. D_L is low.
- The binary merges with the orbital plane face on, i.e. ι is low
- *Both* D_L and ι are low, although this is a small part of the $D_L - \iota$ parameter space and hence is less probable.

This implies a connection between the two parameters, and indeed this $D_L - \iota$ connection is well studied in the literature (see Schutz 2011 & Seto 2015 for discussions on the same). This relation is also important for joint EM-GW observations since the EM signals are inversely proportional to the distance to a binary merger which may produce the prompt emission, whereas the GW signal is sensitive to the inclination angle. This behaviour of the GW SNR was verified to hold within the population generated, which is shown in Fig. 2.7. Note that some parts of the $D_L - \iota$ parameter space are not at all populated by the samples, which reaffirms the fact that distant, edge-on mergers are disfavoured when such systems are being explored via GW.

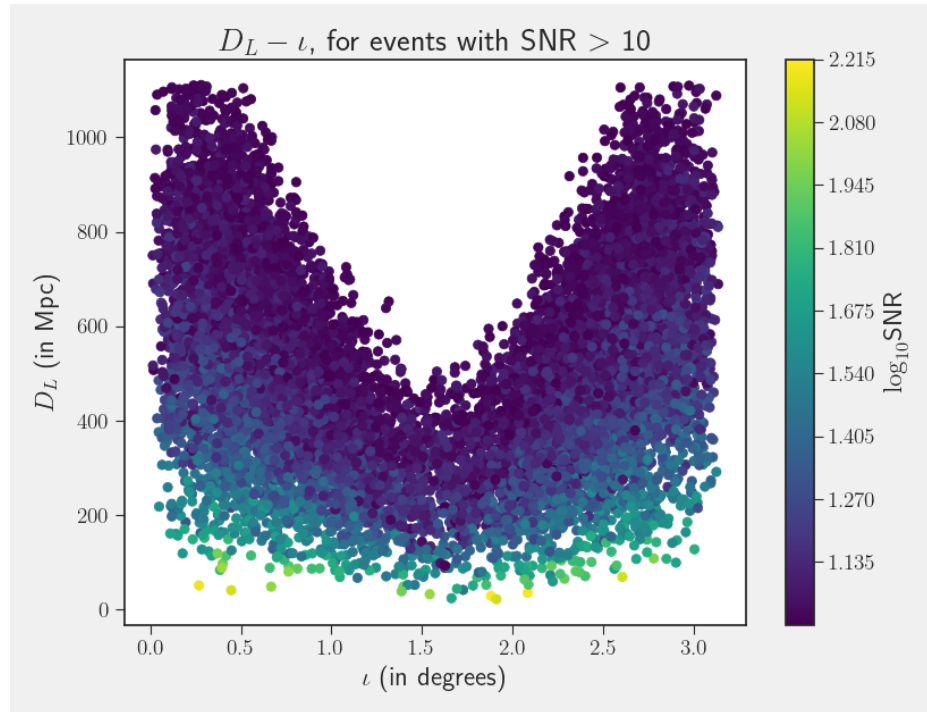


Figure 2.7: Plot of the luminosity distance v/s the inclination angle for events in the population, color coded by the SNR. Note that only events whose $\text{SNR} > 10$ (the SNR threshold) are considered here. This shows that the generated population also exhibits the relation as expected from theory.

2.4.2 EM Checks

The only EM component which has to be validated is the code which imposes the jet structure (Eq. 1.20 – 1.22), once the energetics of the jet are computed via Eq. 1.13 – 1.15.

In order do this, one extracts the θ_v samples from the generated population, which can be done using the relation $\theta_v = \min(\iota, \pi - \iota)$. Then, a common baseline is achieved by setting the value of $E_{kin,jet} = 10^{49}$ erg for all samples, regardless of the actual value if the binary parameters were to be taken into consideration. This is necessary to *remove* the variation of the structure with the intrinsic jet energetics, which is intimately related to the binary parameters.

Then with this constraint applied, the value of $E_{iso}(\theta_v)$ is computed using Eq. 1.20 – 1.22. It is seen from Fig. 2.8 that jet structure is being imposed correctly and according to what is expected from theory.

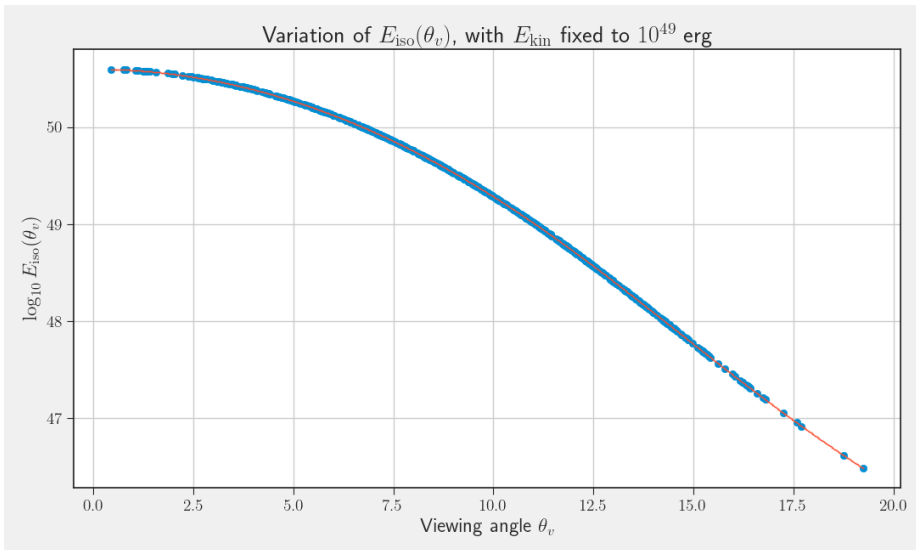


Figure 2.8: Validation of the jet structure code, using the process mentioned in text. The blue scatter points are the values computed for $E_{iso}(\theta_v)$ for parameters from a population with $E_{kin,jet}$ set to 10^{49} erg, whereas the red line is that computed from theory for a jet with the same kinetic energy.

One additional check was performed to confirm the distribution of simulated, jet launching binary mergers. The number of mergers which launched a jet with a fluence greater than some particular value ($\mathcal{N}(> \mathcal{F})$) was plotted, as a function of the particular fluence value(\mathcal{F}).

If the jet structure and spatial distribution codes were working to mimic what is

observed in reality, the resulting structure should be isotropic but inhomogenous, since the sources would be cosmological in nature but appear isotropically distributed in the local universe. As for the expected behaviour of $\mathcal{N}(> \mathcal{F})$, it would behave as $\mathcal{F}^{-1.5}$ for large values of \mathcal{F} , but would significantly deviate from this behaviour for smaller values of \mathcal{F} .

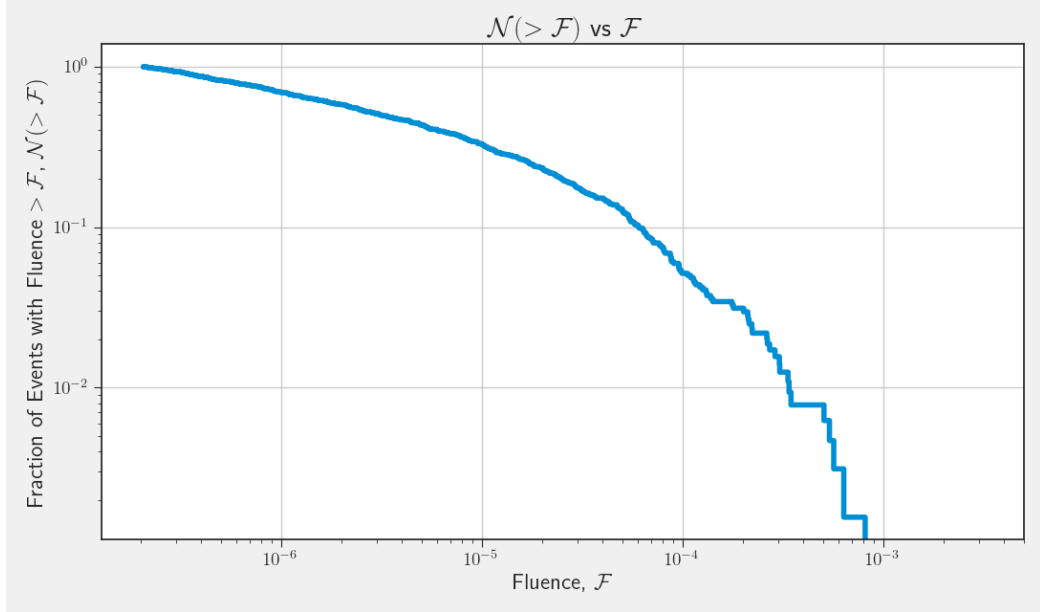


Figure 2.9: Variation of $\mathcal{N}(> \mathcal{F})$ with the fluence \mathcal{F} . Note the significant deviation of this function from the $\sim \mathcal{F}^{-1.5}$ behaviour at lower values of the fluence.

From Fig. 2.9, it is seen that the distribution of simulated mergers which launch a jet mimics the observed distribution of SGRBs in the Universe, and so the jet structure and spatial distribution codes are satisfactory.

As an additional check for the jet structure and energetics code, a few prototypical binary mergers are considered, where each prototype is identified by the mass ratio, \mathcal{Q} , which is varied as $\mathcal{Q} = \frac{3}{1.4}, \frac{5}{1.4}, \frac{10}{1.4}$. The variation of the fluence with the black hole spin, χ_{BH} and the viewing angle, θ_v is what is studied in each prototypical case. These are given in Figs. 2.10 – 2.11.

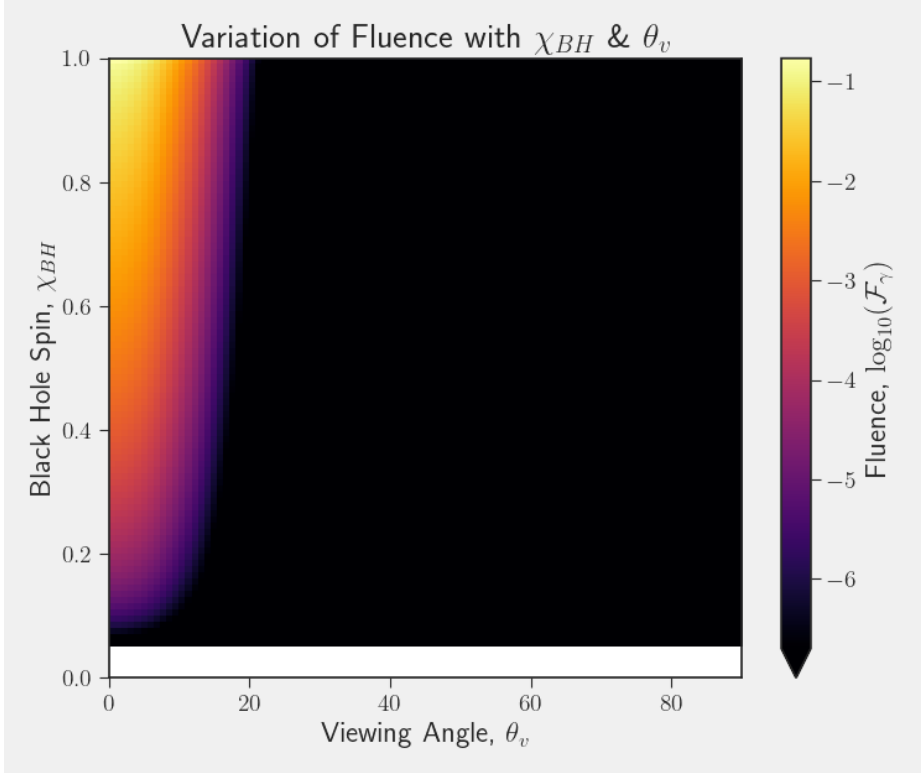


Figure 2.10: The variation of fluence with the viewing angle and the black hole spin for a binary merger with a mass ratio of $\mathcal{Q} = 3 : 1.4$. Here the regions of the $\chi_{BH} - \theta_v$ parameter space in white are those regions where no disc is produced, and hence the outgoing fluence is 0.

A few important points are readily visible from careful observation of the Figs. 2.10 – 2.11, which will be useful for the discussion in subsequent chapters:

- The higher the mass ratio of the merging NSBH system, the lower the probability for a jet to be launched. This is because the inspiralling NS plunges into the BH more often than not, thus undergoing little to no tidal disruption. Thus, the possibility of disc formation, and thus jet launching is very low in very asymmetric binaries.
- With asymmetric binary mergers, only if the black hole spin is high enough will there be any possibility of jet launching. This is because with a high enough black hole spin, the inspiralling NS can become tidally disrupted, and thus a massive disc can be formed using which a jet can be launched. However, it is highly unlikely that such high black hole spins are actually physical.

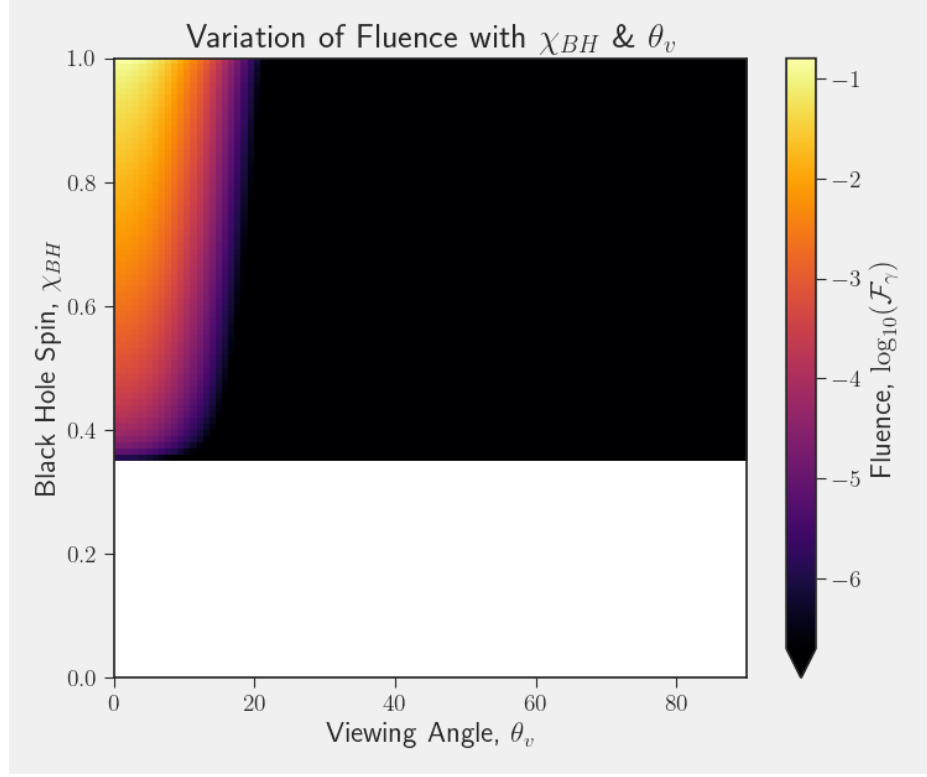


Figure 2.11: The variation of fluence with the viewing angle and the black hole spin for a binary merger with a mass ratio of $\mathcal{Q} = 5 : 1.4$. Note that in this case the region where a disc is not produced is a much larger fraction of the parameter space, compared to Fig.2.10.

Thus, from Figs.2.10 – 2.11, it can be seen that symmetric binary mergers will produce much brighter jets for a given black hole spin, and these jets will be seen out to higher viewing angles. This fact will be useful while discussing the analysis of the various populations synthesized, along with their EM/GW/joint detectabilities. Furthermore, from these figures, it is also verified that the code which imposes the jet structure and energetics is working correctly, since these conclusions about the EM detectabilities of NSBH binary mergers are the ones corroborated by literature as well (see 1.2 for a brief overview of the literature discussing these results).

2.5 Summary

In this chapter, the various populations that will be used to probe the EM counterparts of NSBH mergers were introduced. Along with this, a summary of the various tests carried out was given, wherein the tests made sure that the internal codes that

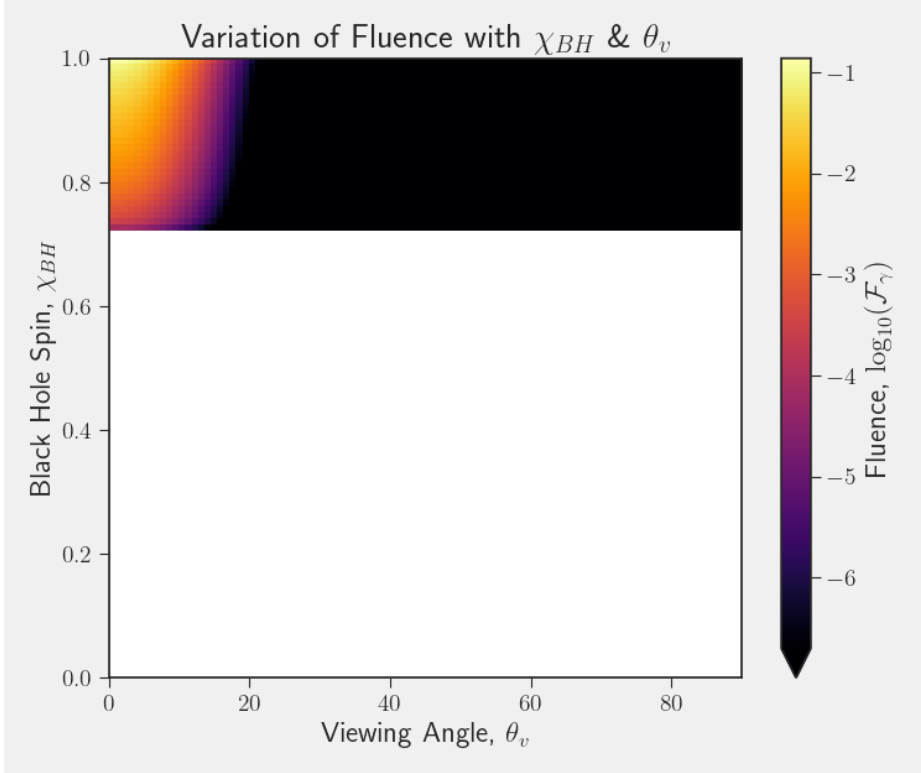


Figure 2.12: The variation of fluence with the viewing angle and the black hole spin for a binary merger with a mass ratio of $\mathcal{Q} = 10 : 1.4$. Here the region of parameter space where the jet is launched is extremely restricted, as the NSBH binary in question is extremely asymmetric in its masses.

compute GW SNRs, calculate jet energetics (from formulae derived as fits to numerical relativity simulations), impose jet structures etc., gave preliminary results which align with the theoretical results.

In the coming chapters, the framework set up in this and the previous chapters for the synthesis of the populations, will be used to analyse the generated populations and the resulting NSBH merger events will be used to derive results about the properties of these binary mergers, and their subsequent prompt EM counterparts.

Chapter 3

NS Merger Candidates in GWTC-2

3.1 About GWTC-2

The first half of the third observing run (O3a) of the LVC started on the 1st of April 2019, and went on till 30th of September, 2019. Following this, instrumental upgrades were made during the month of October and the second half of the third observing run (O3b) was started on the 1st of November. Due to the global pandemic, the observing run had to be prematurely suspended on 30th of March, 2020.

Starting with O3, alerts were distributed via the public alerts section of Gravitational-wave Candidate Event Database (GRACE-DB). If triggers were registered that passed the detection threshold of the LVC network during observational runs, online parameter estimation was done using the raw GW data, and low latency estimates of the rough sky position, component masses and luminosity distance was made available for observers in the EM regime. This allowed for rapid follow-up in various bands of the electromagnetic spectrum, and these observations were reported and cross-verified using NASA’s GRB Coordinates Network (GCN). Using the circulars reported in the GCN for NSBH/BNS events of interest, along with the low-latency information from GRACE-DB, O3a’s non-BBH candidate events have been collected in table 3.3.

More detailed analysis of these events in the months following has led to at least 53 events in the third observing run alone. These can be classified as:

- 37 Binary Black Hole (BBH) merger candidates.
- 7 BNS merger candidates. Of these, only 1 corresponds to O3a, which is the event GW190425 discussed in the chapter 3.2.
- 4 events in the mass gap, which are events with compact objects with masses of $3\text{-}5 M_{\odot}$.

- 5 NSBH merger candidates. Of these, only 1 has been confirmed officially, which is the event GW190814.

Of these, 26 events were officially confirmed and 13 new events were reported for the first time in R. Abbott et al. 2020, and it is from there that the posterior distributions of the various parameters (such as inclination angle ι , luminosity distance D_L etc) are used for further analysis. Note also that there are several marginal events that have been reported, in that they have non-negligible probability distributed between two classifications. For example, the event GW190426_152155 has significant probability split between it being a terrestrial event (58 %) and a NSBH/BNS/Mass Gap event (cumulatively 42%). Without a significant EM counterpart, this event cannot be confidently placed in either of the classes, and thus warrants further analysis. This is the subject of §3.3.

| GRACE-DB | | | | | | |
|-----------------|---------------------------|---------------------------|-------------------------------|----------------------------|----------------------------|--|
| Superevent | $\mathcal{P}(\text{BBH})$ | $\mathcal{P}(\text{BNS})$ | $\mathcal{P}(\text{MassGap})$ | $\mathcal{P}(\text{NSBH})$ | $\mathcal{P}(\text{Terr})$ | |
| ID | | | | | | |
| <u>S190426c</u> | 0 | 24 | 12 | 6 | 58 | |
| S190910h | 0 | 61 | 0 | 0 | 39 | |
| S200213t | 0 | 63 | 0 | 0 | 37 | |
| S191213g | 0 | 77 | 0 | 0 | 23 | |
| S190901ap | 0 | 86 | 0 | 0 | 14 | |
| <u>S190425z</u> | 0 | >99 | 0 | 0 | 0 | |
| S190930s | 0 | 0 | 95 | 0 | 5 | |
| S190923y | 0 | 0 | 0 | 68 | 32 | |
| S190930t | 0 | 0 | 0 | 74 | 26 | |
| S191205ah | 0 | 0 | 0 | 93 | 7 | |
| S190910d | 0 | 0 | 0 | 98 | 2 | |
| S190814bv | 0 | 0 | 0 | >99 | 0 | |

Table 3.1: List of candidate merger events and the probability of classification (reported in %) for each non-BBH event reported during O3a. Here the GRACE-DB superevent ID is used (instead of the GWTC-2 event ID), since for a particular GW event, the superevent collects both the EM followup as well as GW trigger information within GRACE-DB. The probabilities are assigned using the process described in Kapadia et al. 2020, and are reported in GRACE-DB. The events underlined are discussed in more detail in later chapters.

| UID | FAR | D_L (Mpc) | Error in D_L (Mpc) |
|-----------------|-----------------------|-------------|----------------------|
| S190426c | 1 per 1.6276 yr | 377 | 100 |
| S190910h | 1.1312 per yr | 230 | 88 |
| S200213t | 1 per 1.7934 yr | 201 | 80 |
| S191213g | 1.1197 per yr | 201 | 81 |
| S190901ap | 1 per 4.5093 yr | 241 | 79 |
| <u>S190425z</u> | 1 per 69834 yr | 158 | 43 |
| S190930s | 1 per 10.534 yr | 709 | 191 |
| S190923y | 1.5094 per yr | 438 | 133 |
| S190930t | 1 per 2.0536 yr | 108 | 38 |
| S191205ah | 1 per 2.5383 years | 385 | 164 |
| S190910d | 1 per 8.5248 years | 606 | 197 |
| S190814bv | 1 per 1.559e+25 years | 241 | 26 |

Table 3.2: List of candidate merger events and the probability of classification for each non-BBH event reported during O3a. FAR refers to the False Alarm Rate (in number of events per year or equivalently in Hz⁻¹), and D_L is the luminosity distance. Both these values are those reported in GRACE-DB corresponding to each event. The events underlined are discussed in more detail in later chapters.

| UID | FERMI-LAT | FERMI-GBM | SWIFT/BAT | INTEGRAL |
|-----------------|-----------|-----------|--------------|------------------------------|
| S190426c | 24342 | 24248 | 24255 | 24242 |
| S190910h | 25742 | 25714 | 25718 | 25709 |
| S200213t | 27062 | 27056 | 27058 | 27050 |
| S191213g | 26412 | 26409 | 26410 | 26401 |
| S190901ap | 25625 | 25610 | 25617 | 25605 |
| <u>S190425z</u> | 24266 | 24185 | 24184, 24296 | 24169, 24170 24178, 24181 |
| S190930s | 25895 | 25886 | 25889 | 25872 |
| S190923y | 25834 | 25823 | 25846 | 25815, 25825 |
| S190930t | 25898 | 25887 | 25888 | 25880 |
| S191205ah | 26363 | 26359 | 26365 | 26531 |
| S190910d | 25717 | 25699 | 25704 | 25698 |
| S190814bv | 25385 | 25326 | 25341 | 25323 |

Table 3.3: List of candidate merger events and the probability of classification for each non-BBH event reported during O3a. Here the GCN Circular number reporting the findings of the particular instrument in the column heading is reported, corresponding to each event. The events underlined are discussed in more detail in later chapters. GCNs marked with red should be ignored during analysis since they correspond to times when the respective instruments were in the South Atlantic Anomaly (SAA).

3.2 Analysis of GW190425

GW190425 (or S190425z in GRACE-DB) is a GW trigger which was recorded by the LVC on 25th April, 2019 at 08:18 UTC. At the time of this trigger, the Hanford site of LIGO (H1) was undergoing maintenance, whereas the Livingston site (L1) of LIGO and the VIRGO (V1) detector were both operational. However, at the VIRGO detector this event was sub-threshold, effectively making this event a single-detector trigger. As a consequence, the LVC sky localisation area was wider than as compared to GW170817, and EM follow-up was constrained to serendipitous observations by

satellites which happened to be observing the same area of the sky, or to diminished coverage by satellites due to observational schedules. However, online parameter estimation routines computed a greater than 99% probability for the source to be a BNS merger, and so fervent observation campaigns were carried out to observe the sky localisation area as best as possible to look for a prompt or Kilonova signal, similar to what was seen for GW170817.

Initial work was carried out to reproduce the results of M. Saleem et al. 2020, where the authors use a frequentist approach to discuss the possibility of a relativistic jet from the binary neutron star (BNS) merger event GW190425¹. In M. Saleem et al. 2020, three key ideas are developed which are described in detail in the following sections.

3.2.1 Constraints on the $D_L - \iota$ Posterior

At the time of writing of M. Saleem et al. 2020, only the low-latency information was made public. Consequently, information about the inclination angle of this event was not released. However, both the luminosity distance (D_L) and inclination angle (ι) of the event are required for the electromagnetic analysis of the event². To solve this issue, a known correlation between the luminosity distance D_L and ι (see Schutz 2011, Seto 2015) was used to infer the distribution of ι for this event, which was possible since the former was publicly known.

The following are the other publicly released information relevant to the problem, and can be used to constrain the $D_L - \iota$ joint distribution:

- The posterior probability of the event being a BNS merger is $> 99\%$,
- The event was observed by the LIGO Livingston (L1), and Virgo (V1) detectors, whereas the LIGO Hanford (H1) detector was not observing. However, at V1 the signal-to-noise ratio (SNR) was below the threshold and thus this event was a single detector trigger.
- The preliminary luminosity distance estimate is given by $D_L = 155 \pm 41$ Mpc.

¹At the time of the writing of the paper, this event was still not confirmed as a bona-fide GW event, and so it was denoted by GRACE-DB as S190425z. Consequently, several key pieces of information (such as the luminosity distance and inclination angle posteriors) from the GW inference were not yet public, and had to be worked around. See text for more details.

²The former is used to calculate the fluence, and the latter is directly related to the viewing angle, which in turn decides the observed isotropic equivalent energy (see Eq. 3.1)

Using these inputs the $D_L - \iota$ space is constrained as follows.

1. A population of BNS mergers is simulated, such that they are uniformly distributed in the comoving volume, with the inclination angle of the binaries being such that $\cos \iota \in [-1, 1]$. This also means that the luminosity distance is initially distributed such that $\mathcal{P}(D) \propto D^2$ upto some threshold distance. For the purposes of the simulations, this threshold distance is set to be the distance corresponding to the 99% percentile of a Gaussian with a mean of 155 Mpc and a standard deviation of 41 Mpc. In practice, it is the maximum distance up till which the comoving and the luminosity distances can be used interchangeably, which corresponds to a redshift of roughly 0.1.
2. The NS masses are uniformly distributed between $1\text{--}2 M_\odot$. This enforces the constraint that from the analysis of the GW waveform, the event has $> 99\%$ probability of being a BNS merger.
3. Then, the optimal SNR is computed for each realisation using the restricted post-Newtonian (PN) waveform (RWF) (see Cutler and Flanagan 1994, Kastha, Saleem, and Arun 2020), and the Eqs. 2.9 – 2.13. To compute the optimal SNR in L1 and V1, the best reported O2 sensitivities were used as conservative O3 sensitivities, as an input for $S_h(f)$. As the trigger is an L1 single-detector trigger, the conditions that $\text{SNR} < 4$ at V1 and the network $\text{SNR} > 9$ are enforced. The former is motivated by the single-detector threshold of the GstLAL pipeline, whereas the latter is motivated by the fact that the network SNR of all O1/O2 events was > 9 .
4. From the resulting population, a sub-population is extracted such that the luminosity distance follows a Gaussian distribution with a mean of 155 Mpc and a standard deviation of 41 Mpc. This is done so as to impose the constraint applied by the luminosity distance posterior distribution released by the LVC.

The resulting 2D distribution of $D_L - \iota$ of this sub-population is shown in Fig. 3.1 below. This is used further on, as the prior for studying the possibility of a SGRB from GW190425.

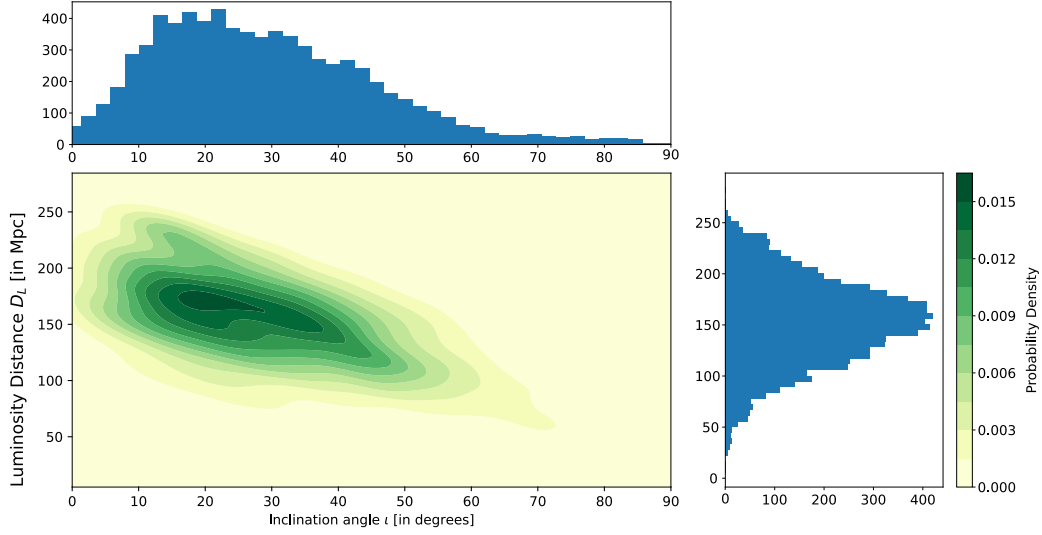


Figure 3.1: Constraints on the $D_L - i$ joint distribution, obtained from imposing the observed properties of S190425z/GW190425.

3.2.2 Calculation of the Apparent structure

Assuming the intrinsic jet structure models described before (in Sec. 1.1), the apparent isotropic equivalent energy is calculated using the equation (as in Salafia et al. 2015 and Biscoveanu, Thrane, and Vitale 2020):

$$E_{iso}(\theta_v) = \frac{1}{2\pi} \int_0^{2\pi} d\phi \int_0^{\theta_{max}} d\theta \sin \theta \frac{\epsilon(\theta)}{\Gamma(\theta)^4 [1 - \beta(\theta) \cos \alpha_v]^3} \quad (3.1)$$

where:

- θ_v is the viewing angle of the observer.
- $\epsilon(\theta)$ is the normalised energy profile function.
- α_v is the angle between the line of sight and the direction to the jet element at (θ, ϕ) , given by $\cos \alpha_v = \cos \theta_v \cos \theta + \sin \theta_v \sin \theta \cos \phi$.
- θ_{max} is the upper cut-off of polar integration³.

Thus, depending on the underlying intrinsic structure assumed (be it Gaussian or tophat jet), using Eq. 3.1 one can infer the apparent structure of the jet. Note that

³Such a cutoff can occur because the edge of the jet has been reached, or that the gamma-ray emission efficiency is lowered above a threshold, and so emission is negligible beyond θ_{max} .

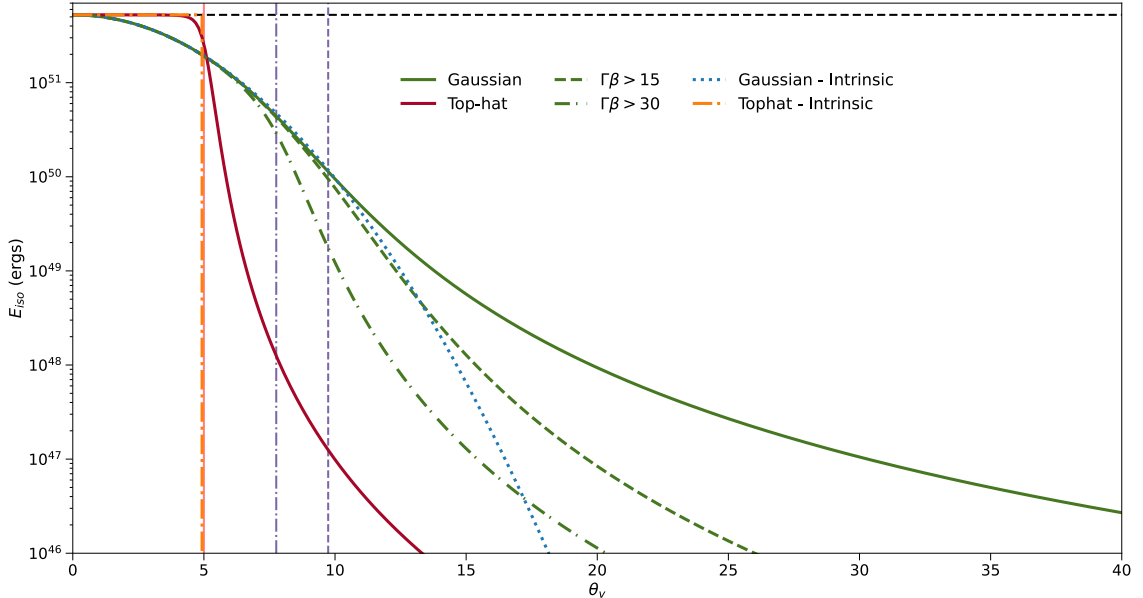


Figure 3.2: Variation of the apparent isotropic equivalent energy, for observers at different viewing angles. The figure shows both the top-hat (dark red) and Gaussian (dark green) jet structures, with $E_{tot,\gamma} = 10^{49}$ ergs. θ_j for the top-hat jet and θ_c for the Gaussian jet are both 5° (marked with vertical solid bright red line), and Γ_0 in both cases is 100. The horizontal dashed black line denotes $E_{iso}(0)$. The orange, dash-dotted line and the blue dotted lines are the tophat and Gaussian intrinsic jet structures, represented as $4\pi\epsilon(\theta_v)$. For the solid green curve, the entire jet emits gamma-rays, whereas for the dashed and dash-dotted green curves the emission is restricted to regions where $\Gamma\beta > 15$ and $\Gamma\beta > 30$, leading to limits in the polar integration of 9.74° (vertical dashed violet line) and 7.76° (vertical dash-dotted violet line) respectively.

this is the variation of the (apparent) isotropic equivalent energy (E_{iso}) at various viewing angles (θ_v), and hence gives how the SGRB jet, if launched, would appear to an observer at an angle to the jet's axis. This variation is shown in Fig. 3.2, and is used a prior for further analysis.

3.2.3 Monte-Carlo simulations

Using the information from previous analyses and the priors motivated from them, a Monte-Carlo simulation was carried out where 10^5 realisations of the Gaussian jet were made. Their model fluence was compared with what was reported by INTErnational Gamma-Ray Astrophysics Laboratory (INTEGRAL).

Around the time of the GW trigger, INTEGRAL was observing the entire Ad-

vLIGO/VIRGO localisation region and according to Minaev et al. 2019, saw a low SNR short duration (~ 1 s) excess roughly 6s after the merger. Further analysis reported a fluence of $(1.6 \pm 0.4) \times 10^{-7}$ erg/cm². The priors used for the various parameters of the Gaussian jets realised are as given in table 3.4.

| | $E_{tot.,\gamma}$ (erg) | Γ_0 | θ_c |
|--------------------------------------|---|---------------------------------------|--|
| Uniform Energy Prior | $\log_{10}(E_{tot.,\gamma}) \sim \mathcal{U}(44, 51)$ | $\Gamma_0 \sim \mathcal{U}(5, 500)$ | $\theta_c \sim \mathcal{U}(3^\circ, 20^\circ)$ |
| Broken Power Law Energy Prior | See Eq. 3.2 below. | $\Gamma_0 \sim \mathcal{U}(100, 500)$ | $\theta_c \sim \mathcal{U}(3^\circ, 20^\circ)$ |

Table 3.4: Priors on the total energy emitted in gamma-rays ($E_{tot.,\gamma}$), bulk on-axis Lorentz factor (Γ_0) and core-angle (θ_c). The form of the broken power law used here is given in text.

Here, the broken power law energy prior is given by:

$$P(E_{tot.,\gamma}) \propto \begin{cases} E_{tot.,\gamma}^{-0.53}, & 5 \times 10^{47} \text{ ergs} < E_{tot.,\gamma} < 10^{50} \text{ ergs} \\ E_{tot.,\gamma}^{-3.5}, & 10^{50} \text{ ergs} < E_{tot.,\gamma} < 5 \times 10^{51} \text{ ergs} \end{cases} \quad (3.2)$$

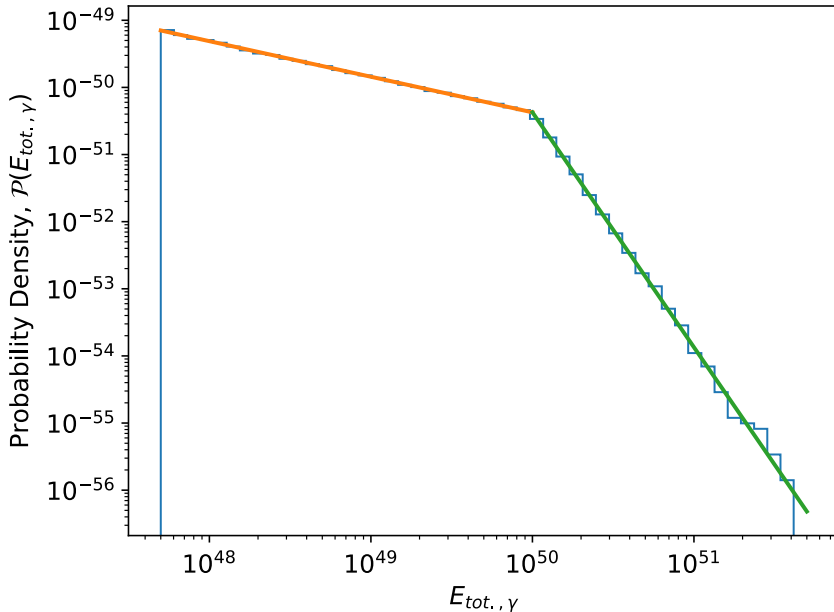


Figure 3.3: The broken power law distribution as described in Eq. 3.2.

This particular distribution for the prior of $E_{tot,\gamma}$ is adopted since it is able to reproduce the fluence distribution observed for values above the limiting fluence of 2×10^{-7} erg/cm² (see Mohan, Saleem, and Resmi 2019). Furthermore, the power-law indices are adopted from the luminosity function described in Ghirlanda et al. 2016.

In applying these priors, along with the $D_L - \iota$ prior and the fluence values of 2×10^{-7} and $(1.6 \pm 0.4) \times 10^{-7}$ erg/cm² as upper limit and observed fluence supplied by INTEGRAL respectively, the marginalized posteriors for $\theta_c, \Gamma_0, \theta_v$ and $E_{tot,\gamma}$ are obtained. These are converted into $E_{iso}(0)$. The posterior distributions of the on-axis, apparent isotropic equivalent energy, for the two priors considered, is shown in Fig. 3.4. As is evident from seeing the figure, the INTEGRAL fluence is a good constraint for the priors. For the uniform prior case, considered as a detection, the posterior $E_{iso}(0)$ is tightly constrained to be between $3.51 \times 10^{47} - 6.26 \times 10^{52}$ ergs, which shows that for an on-axis observer, the event would have appeared as a typical SGRB along with the GW event. Even considering as an upper-limit constrains $E_{iso}(0) \leq 1.48 \times 10^{51}$, which is broadly in agreement with that observed for typical SGRBs. On the other hand, the narrower, broken power-law prior is not constrained well with the INTEGRAL fluence. Considered as a detection, the 90% credible posterior bounds on $E_{iso}(0)$ are $1.17 \times 10^{49} - 1.3 \times 10^{51}$ ergs, whereas considered as an upper limit, $E_{iso}(0) \leq 7.69 \times 10^{50}$ erg. In both cases, the posteriors are sensitive to the choice of the prior, but nevertheless, one cannot rule out an SGRB jet which would have been seen by an on-axis observer.

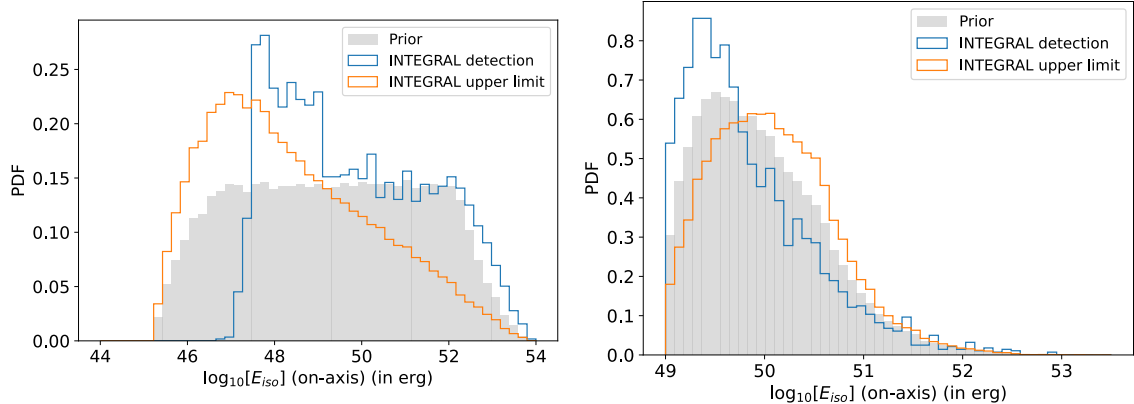


Figure 3.4: Posterior distributions of the apparent on-axis isotropic equivalent energy $E_{iso}(0)$, for two assumed priors on the total energy emitted in gamma-rays, $E_{tot,\gamma}$. These figures give constraints on the $E_{iso}(0)$ of the SGRB associated with GW190425, assuming a Gaussian structured jet. **Left:** Grey histogram indicates the uniform priors on $\log_{10}(E_{tot,\gamma}/\text{erg})$ in the range of [44 – 51], and on θ_c in [3, 20] degrees. **Right:** the same prior is used for θ_c but a broken power law prior is used for $E_{tot,\gamma}$. The orange histograms in both are a result of considering an INTEGRAL fluence upper limit of $2 \times 10^{-7} \text{ erg/cm}^2$, where the blue histograms in both are a result of considering an INTEGRAL fluence detection of $(1.6 \pm 0.4) \times 10^{-7} \text{ erg/cm}^2$. In both cases, the on-axis energy of a possible associated GRB is within the range of that of the cosmological SGRB population.

3.2.4 Using LIGO posteriors

In the time since the analysis in M. Saleem et al. 2020 was carried out, the posteriors for the O3a events were released as part of the Gravitational Wave Transient Catalog (GWTC) 2 (see R. Abbott et al. 2020). These are now available as part of the event portal at the Gravitational Wave Open Science Center (GWOSC), which lists the files that store samples from posterior distributions for various parameters, for each event in GWTC-2. This allows one to use the actual posteriors for the inclination angle and the luminosity distance reported by the LVC. These are plotted in Fig. 3.5, below.

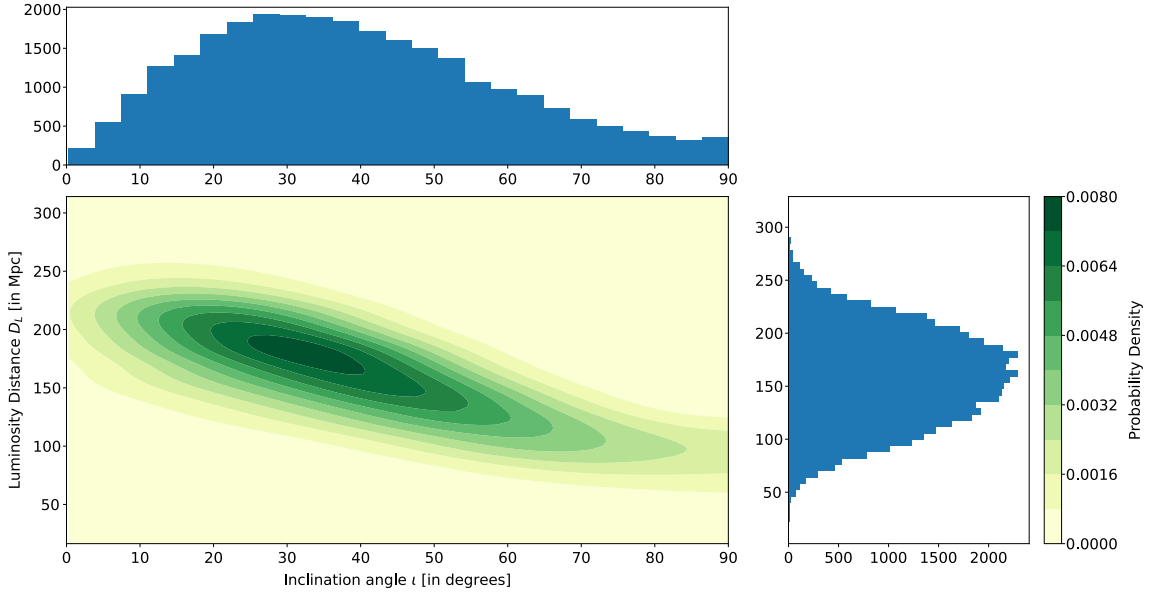


Figure 3.5: Similar as 3.1, but with samples for D_L and ι from the posteriors released by the LVC, as part of the GWTC-2 data release.

These posteriors for the parameters ι and D_L will be more accurate than the ones generated in §§3.2.1, since those posteriors are generated by approximating the O3a detector noise curves using the conservative best estimate from O2. Hence using the actual detector noise around the time of the event , performing parameter estimation for the parameters of interest (which is done by LVC), and using the resultant posteriors will be more accurate for further analysis.

Using these posteriors, the constraints on the energetics of a SGRB jet being powered by an event like GW190425 change slightly. This is shown in Fig. 3.6.

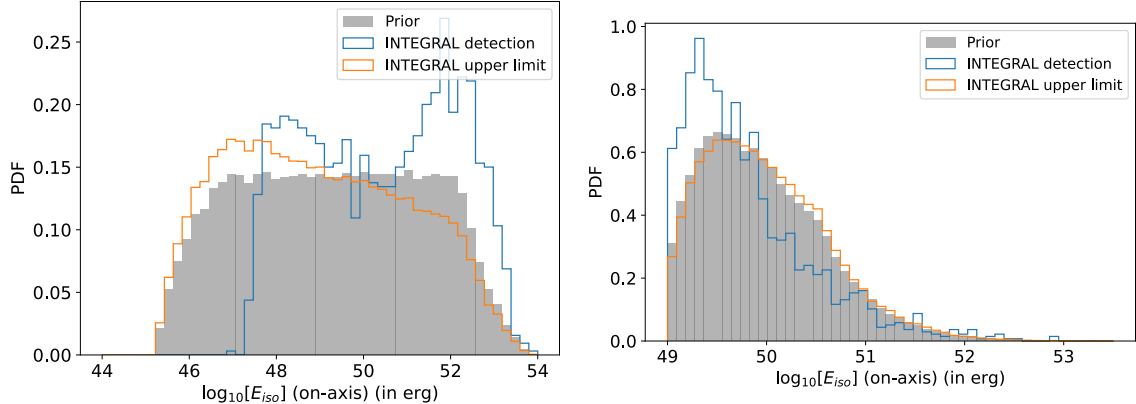


Figure 3.6: Posterior distributions of the apparent on-axis isotropic equivalent energy $E_{iso}(0)$, with similar priors as Fig. 3.4 but with LVC posterior samples as input.

Considering the INTEGRAL fluence as a detection, the posterior bounds on $E_{iso}(0)$ are $5.61 \times 10^{47} - 8.48 \times 10^{52}$ ergs. This again leads to the conclusion that for an on-axis observer, the SGRB jet would have appeared similar to one from the cosmological population. Considering the INTEGRAL fluence as an upper limit instead, gives that $E_{iso}(0) \leq 7.43 \times 10^{51}$ erg. Similar to the previous case, the narrow broken-power law prior is not well constrained by the INTEGRAL fluence limits, which places the bounds $1.15 \times 10^{49} - 1.11 \times 10^{51}$ ergs (considered as a detection) and $E_{iso}(0) \leq 6.74 \times 10^{50}$ erg (considered as an upper limit). In this case as well, the conclusion is the same, that the possibility of an SGRB jet which would have been visible seen on-axis cannot be ruled out. However, this showcases the usefulness of the method described in §3.2.1, wherein the posterior for the parameter ι can be approximated and used for further analysis, without having to wait for this information to be released officially.

3.3 Preliminary analysis of GW190426_152155

The event GW190426_152155 is listed in GWTC-2 (R. Abbott et al. 2020) as an event with a network matched filter SNR of 10.1, a false-alarm rate of 1 event per 1.6276 yr and the component masses are $5.7_{-2.3}^{+4.0} M_\odot$ and $1.5_{-0.5}^{+0.8} M_\odot$. From GRACE-DB, this event has probabilities 0.58, 0.24, 0.12, 0.06 respectively of being a Terrestrial, BNS merger, NSBH merger or Mass Gap merger event.

Although there were no significant excesses reported by any of the gamma-ray satellites observing the LVC localisation area at the time of the GW trigger, the INTE-

GRAL satellite reported an upper limit fluence of 1.7×10^{-7} ergs/cm². With the priors as given in Table 3.4, this fluence upper limit reported by INTEGRAL is taken as the primary constraint. Similar to the process described in §3.2.3, 10^5 realisations of the jet are made, the apparent on-axis isotropic equivalent energy calculated, from which the fluence is computed and those realisations with a fluence beyond the upper limit are rejected. The resulting population has a distribution as given in Fig. 3.7. As can be seen from Fig. 3.7, at apparent on-axis isotropic equivalent energies below 10^{48} erg, the uniform energy prior differs appreciably from the posterior, whereas at higher energies the posterior and prior exhibit the same behaviour. However, in the case of the broken power-law energy prior, at all energies considered the posterior and prior distributions are similar. Hence the fluence upper limit offered by INTEGRAL doesn't offer tight constraints.

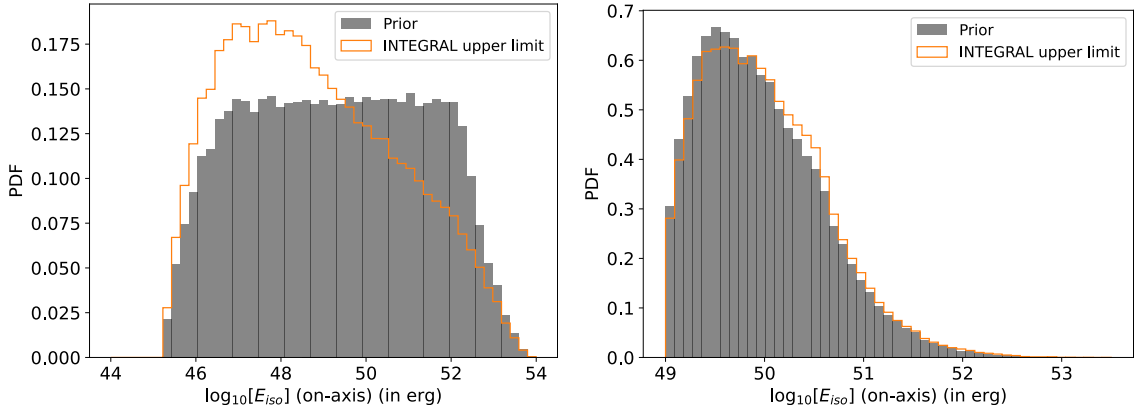


Figure 3.7: Posterior distributions of the apparent on-axis isotropic equivalent energy $E_{iso}(0)$, for two assumed priors on the total energy emitted in gamma-rays, $E_{tot,\gamma}$. These figures give constraints on the $E_{iso}(0)$ of the SGRB associated with GW190426_152155, assuming a Gaussian structured jet. **Left:** Grey histogram indicates the uniform priors on $\log_{10}(E_{tot,\gamma}/\text{erg})$ in the range of [44 — 51], and on θ_c in [3, 20] degrees. **Right:** the same prior is used for θ_c but a broken power law prior is used for $E_{tot,\gamma}$. The orange histograms in both are a result of considering an INTEGRAL fluence upper limit of 1.7×10^{-7} erg/cm².

This process hence tests to see whether the models used for the analysis of GW190425, also apply to an NSBH event GW190426_152155. Although the constraint is not very good in either case of the prior, the conclusion is that there is a possibility of a SGRB jet which would have been detected had the observer been on-axis. In this case, considering the constraint as an upper limit, the bounds are $E_{iso}(0) \leq 4.52 \times 10^{51}$ erg and $E_{iso}(0) \leq 6.81 \times 10^{50}$ erg for the uniform prior and

the broken power-law prior respectively. As an additional check, Table 3.5 lists the parameters for some of the typical, well-studied SGRBs. Comparing what was obtained after the analysis of GW190426_152155 to the observed isotropic equivalent energy for these SGRBs, it can be seen that this NSBH event is still in the ballpark of cosmological SGRBs.

| GRB ID | Relevant GCN Notices | Duration (ms) | Fluence (erg/cm ²) | Redshift | Lum. Dist (Mpc) | E_{iso} (ergs) |
|--------------|----------------------------|------------------|--------------------------------------|----------|--------------------|---|
| GRB20050509B | 3385, 3390 | 30 | $2.3^{+0.9}_{-0.9} \times 10^{-8}$ | 0.226 | 1133.2 | $3.53^{+1.38}_{-1.38} \times 10^{48}$ |
| GRB20130603B | 14741, 14744 | 180 | $(6.3^{+0.3}_{-0.3}) \times 10^{-7}$ | 0.356 | 1911.9 | $2.76^{+0.044}_{-0.044} \times 10^{50}$ |
| GRB20160821B | 19844, 19846 | 480 | $(1.0^{+0.1}_{-0.1}) \times 10^{-7}$ | 0.162 | 781.8 | $7.31^{+0.73}_{-0.73} \times 10^{48}$ |

Table 3.5: List of typical cosmological SGRBs and their source parameters. The luminosity distance was calculated from the redshift using a standard cosmology of $H_0 = 69.6$ km/s/Mpc, $\Omega_M = 0.286$ and $\Omega_\Lambda = 0.714$.

3.4 Summary

This chapter introduced the two events of interest in GWTC-2, GW190425 and GW190426_152155, which were analysed thoroughly in this report. The former event was classified as a BNS event by the low-latency parameter estimation, and the framework developed here shows that there is a possibility that a SGRB jet would have been detected from this NSBH merger had the event not been off-axis, with the priors assumed constraining the apparent, isotropic equivalent energy fairly well.

Furthermore, this framework is also extended to the latter event, an event which was classified first as an NSBH signal and then later reclassified to be largely a terrestrial signal, and a similar conclusion is reached regarding the same. However, despite the wide priors, they fail to constrain the apparent isotropic equivalent energy satisfactorily, and so a concrete statement about the nature of the event cannot be reached here. However, this event is revisited in the next chapter where the NSBH-specific framework is applied to shed more light on the nature of this event.

Chapter 4

Event and Population Analysis

Using the population models described in Chapter 2, one can derive the properties of NSBH mergers as seen in the GW and EM regimes. Specifically, an important aspect of NSBH mergers is what fraction of mergers actually produce a prompt component which will be detectable by present-day gamma-ray detectors, such as INTEGRAL. A related aspect is the dependence of this fraction on the priors which go into creating these populations. Specifically, different black hole spin prior distributions would affect the number of detectable prompt emissions, and so this behaviour is worth investigating. Furthermore, this population synthesis framework may also help to investigate the rate density of NSBH mergers which lead to observable SGRBs, which can then be compared to the rate derived currently from purely EM observations. Additionally, events seen solely in the GW regime without any confident EM counterparts may be analysed using the framework set up here. Using the posterior distributions for the component masses, spins etc., derived from GW strain data analysis, one can derive the corresponding remnant, dynamic and disc masses from which the jet energetics can be derived. Under the assumptions of the underlying model, this process of computation can then help eliminate or give credence to the existence of EM counterparts for events observed via GW only.

4.1 Analysis of Population Synthesis Models

From the description of the population models given in Chapter 2, it is clear that there are three classes of populations, segregated by the black hole spin population that is used. Specifically, the three classes of populations are:

- **Class I** – this uses the standard TRUNCATED BH mass distribution with a

constant NS mass of $1.4 M_{\odot}$. The BH spin distribution is the beta distribution from The LIGO Scientific Collaboration et al. 2020, and the NS spin is set identically to 0 for all samples (see §2.2 for reasons on why this assumption is valid). The remaining NS parameters and their computation (such as the NS compactness, tidal deformability etc.) are described in §2.2, and thus omitted for brevity.

- **Class II** – here, the BH spin distribution is assumed to be uniform between [0, 1). The rest of the binary parameter distributions are the same as in Class I.
- **Class III** – here, the BH spin is a "restricted" Gaussian distribution between [0, 1), which means that samples between [0, 1) are taken as is but samples outside of this range are discarded. For the purposes of being general, samples are drawn from distributions with standard deviation, $\sigma = 0.2$ and mean, $\mu = 0.2, 0.5, 0.7$. The rest of the binary parameter distributions are the same as in classes I and II.

For each population, 10^5 samples are drawn from the relevant populations. Using the samples, the various mass parameters required to compute the energetics of the jet are calculated using Eqs. 1.6 – 1.11. Then, using Eq. 1.13 – 1.22, the jet structure is imposed and for each event the value of $E_{iso}(\theta_v)$ is computed. These are then converted into fluences using the equation:

$$\mathcal{F} = \frac{E_{iso}(\theta_v)}{4\pi d_L^2} \quad (4.1)$$

This is done in order to ascertain the detectability of the prompt emission, with a typical gamma-ray detector, such as the INTEGRAL satellite, as a reference. The INTEGRAL satellite has a lower fluence cutoff of 2×10^{-7} erg, and so with respect to this detector, any event with a fluence lower than this value will be considered a non-detection. Albeit this is a tight and somewhat ephemeral restriction, it helps to ascertain the rough number of detections versus non-detections.

Similarly, with the binary parameters set by the sampling process, the GW network SNR is computed with the RWF as the GW template, using Eqs. 2.10 – 2.13. The detector network configuration consisting of Advanced LIGO (LIGO-Livingston, L1 and LIGO-Hanford, H1) and VIRGO (V1) detectors was set up using PyCBC's `detector` module, which builds up the detector locations, antenna pattern functions, location phase factors etc. For all three detectors, the Advanced LIGO Design sensitivity was

used as an approximation for their respective future configurations. This was done, since with the current network configuration, there have been no confident detections of NSBH mergers which have *also* had an EM counterpart.

The results of the simulations are given below, with each population producing a particular number of NSBH binary merger events seen in:

1. The GW regime alone, $\boxed{\mathcal{N}_{GW}}$ – these are events whose GW network SNR is calculated to be higher than the network SNR threshold of 10.
2. The EM regime alone, $\boxed{\mathcal{N}_{EM}}$ – these are events whose simulated gamma-ray fluence is calculated to be above the INTEGRAL fluence limit of 2×10^{-7} erg.
3. The GW *and* EM regimes both, $\boxed{\mathcal{N}_{EM+GW}}$ – these are events which satisfy both the GW and EM ‘cutoffs’, and thus represent joint detections.

These numbers are collected together in Table 4.1 for each population class. From this table it is evident that nature of the spin distribution heavily affects the number of EM-only events, and by extension the number of joint events.

This can be explained by looking at the dependence of M_{disc} on the BH spin, from Eq.1.10, for a fixed mass ratio. Since a highly spinning black hole produces more tidally disrupted material for a given mass ratio than a low spinning black hole, binaries with a higher black hole spin are more likely to produce a more massive disc (assuming not much mass is lost as dynamical mass). This behaviour of M_{disc} is also shown below in Fig. 4.1.

Table 4.1: Number and Kind of Detections across Population Classes

| | \mathcal{N}_{GW} | \mathcal{N}_{EM} | \mathcal{N}_{EM+GW} |
|------------------------|--------------------|--------------------|-----------------------|
| Class I | 28 | 12283 | 9 |
| Class II | 666 | 11274 | 241 |
| Class III $_{\mu=0.2}$ | 25 | 11250 | 6 |
| Class III $_{\mu=0.5}$ | 290 | 11690 | 93 |
| Class III $_{\mu=0.7}$ | 932 | 11468 | 330 |

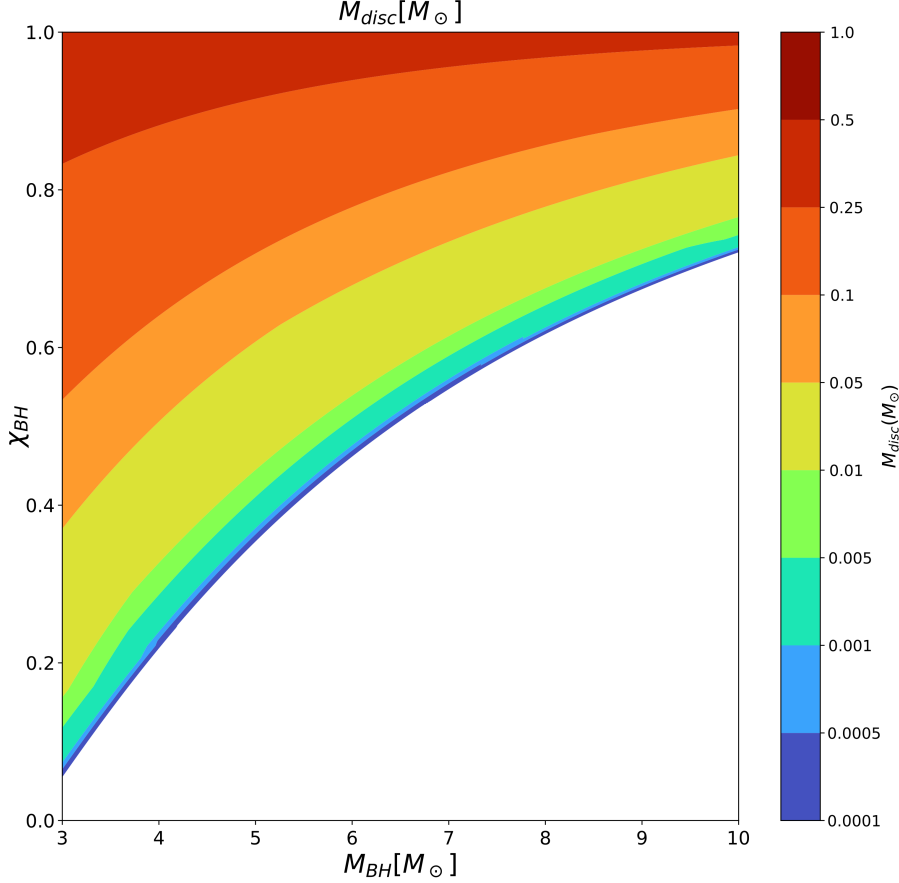


Figure 4.1: Variation of the disc mass with the mass ratio, \mathcal{Q} and the black hole spin, χ_{BH} . Note that the higher disc mass values are achieved when χ_{BH} is high and \mathcal{Q} is low. Reproduced from Barbieri, Salafia, Colpi, et al. 2019.

This then means that because populations with ‘high spin’ distributions (such as Class I or Class III $_{\mu=0.7}$) have a higher proportion of high spin binaries, they have a higher number of EM and joint detections, since a more massive disc produces a more energetic jet from Eq.1.22, and thus increases the possibility of detections.

4.2 Event Analysis

4.2.1 GW190426_152155

This event, as described in GWTC-2 and in §3.3, has an astronomical source probability of 42% and a terrestrial event possibility of 52%. Even though this is the case, there is still speculation on whether this event could be an NS merger event. This is still possible since the priors used for the classification mechanism depend sensitively

on knowledge about the stochastic GW background and the source classification may very well change in the future, as more analysis is done on the GW noise observed as the LIGO/VIRGO interferometers operate.

With this uncertainty in mind, asking the question of whether GW190426_152155 could be an NSBH event is pertinent, and the current framework makes for a suitable test bed to test this hypothesis with. Using the LSC data release for the binary system parameters associated with GW190426_152155, which gives samples from the posterior distributions for M_{BH}, M_{NS} etc., the disc mass was computed for each set of binary parameters. Computing the disc mass is expeditious since it directly gives an estimate of how many sets of samples will be able to *atleast launch* a jet, since if $M_{disc} = 0$ for a particular set of samples, there is no possibility of detecting a jet from this particular binary.

Fig. 4.2 is the result of this analysis in the $\chi_{BH} - Q$ plane. From this figure, it is seen that a minor but non-negligible fraction of posterior samples (32%) actually falls within the section of the parameter space where $M_{disc} \neq 0$. This means correspondingly that the probability of the *NSBH* event GW190426 launching a SGRB jet at all is disfavoured. This can be interpreted trivially to conclude that the event was of terrestrial origin, and thus it follows that it would not be compatible with the launching of an astrophysical jet. But non-trivially, one can also conclude that one of the following is true:

- The event GW190426_152155 was a BNS merger event, which had a jet that was launched via other mechanisms.
- The event GW190426_152155 was an NSBH merger event, but the jet was launched via a mechanism that is unknown. This means that the current analysis is invalid, and the true nature of the jet launching mechanism is unknown.

The actual non-detection of such a jet (if launched under these alternative conditions) could be either due to the inefficiency of the internal engine of such alternative jet launching mechanisms, or due to a viewing angle large enough that the jet was relativistically deboosted to below the thresholds of current-day gamma-ray observatories.

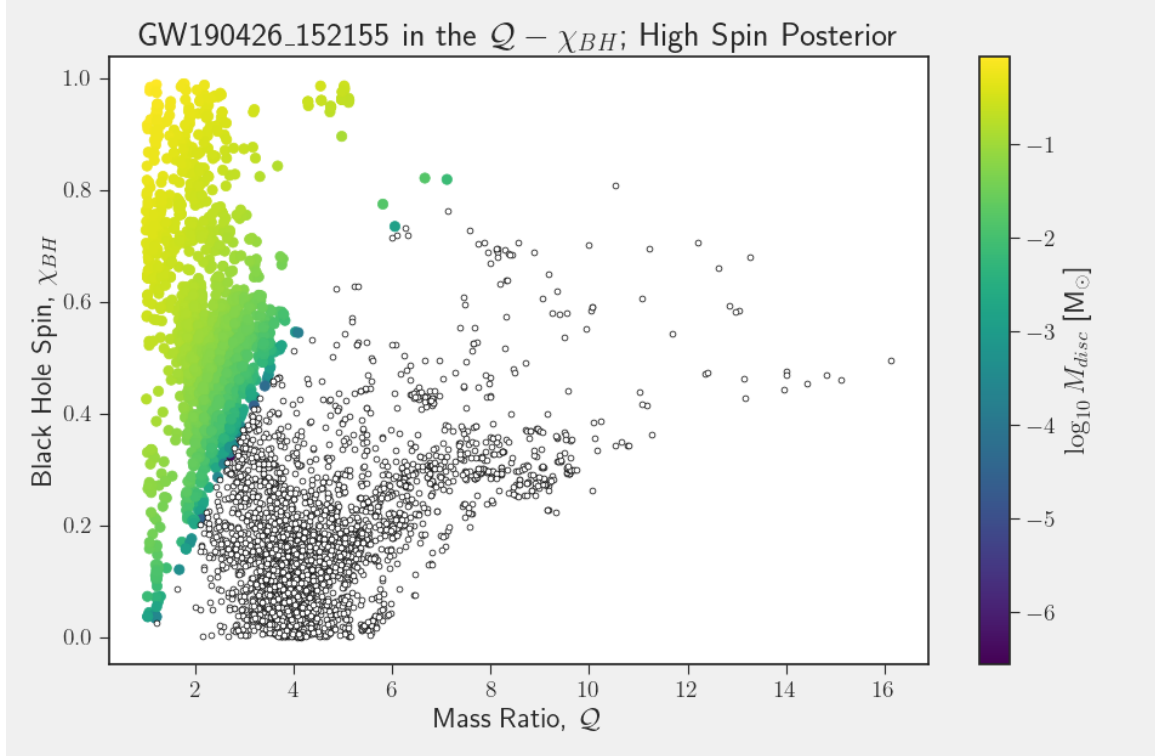


Figure 4.2: GW190426_152155 in the $\chi_{BH} - Q$ plane. The color coding at a point in the plane indicates the value of M_{disc} corresponding to that particular χ_{BH} and Q . Unfilled circles with a black outline correspond to samples from the posterior distributions for GW190426_152155, which have $M_{disc} = 0$, and so cannot support jet launching, and filled black circles are those with $M_{disc} \neq 0$.

4.2.2 GW170817

For GW170817, as described in Chapter 1, a lot of questions remain regarding the specifics of the jet launching mechanisms. Recent studies also show that there is a non-negligible possibility that the event was an NSBH merger, with a low mass BH acting as the other, non-NS component (see for example, Hinderer et al. 2019). This would be compatible with the outflows observed from GW170817, specifically the SGRB jet GRB170817A, optical Kilonova AT2017gfo and associated afterglows (see B. P. Abbott et al. 2017) since NSBH mergers also can produce similar outflows as shown below.

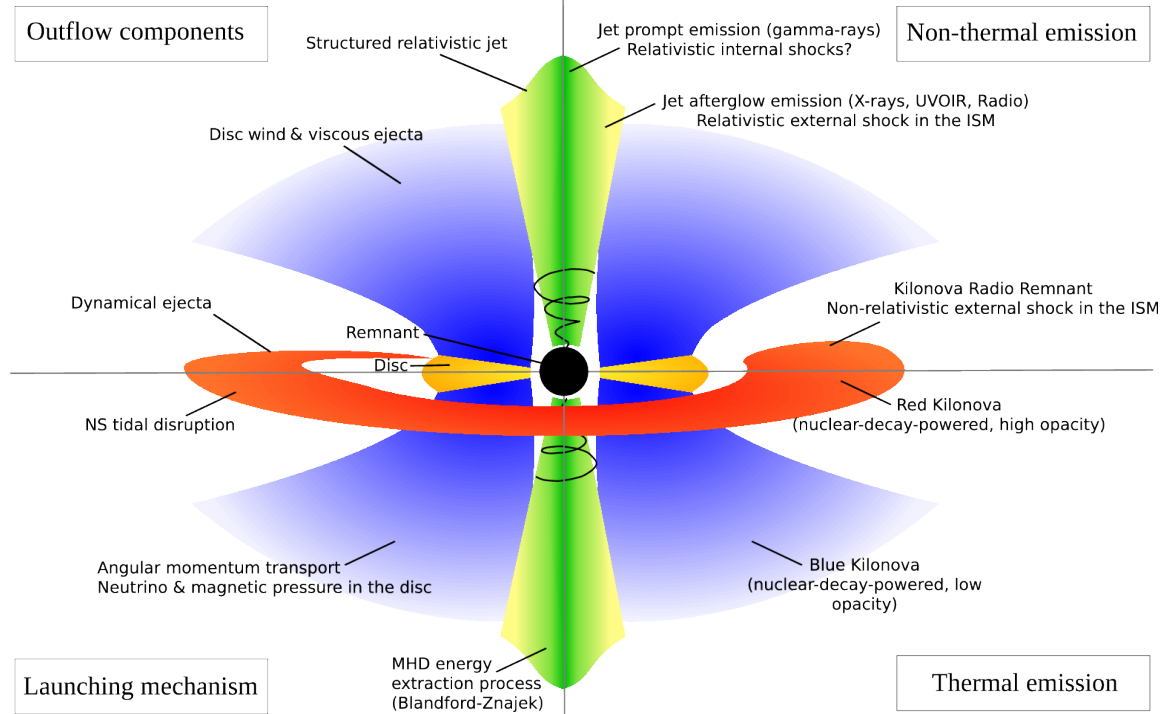


Figure 4.3: Schematic diagram showing the various possible outflows from a suitable NSBH merger, along with their windows of visibility in the EM spectrum, their physical properties and their relevant launching/energy production mechanisms. From Barbieri, Salafia, Perego, et al. 2019.

In order to better understand this event, an analysis similar to that in §§4.2.1 was carried out. The LSC data release for GW170817 (part of the GWTC-1 catalog data release; see LIGO Scientific Collaboration 2018b) was used from which the binary system parameters were extracted. Note that for this data release, there are two ‘flavours’ of posterior distributions which are supplied by the LSC data product, classified by the spin priors used in the Bayesian parameter estimation process. The first is termed `IMRPhenomPv2NRT_highSpin_posterior`¹ whereas the second is termed `IMRPhenomPv2NRT_lowSpin_posterior`, and both are considered in the current analysis.

With the assumption that the heavier mass is the BH and the lighter mass the NS, the mass ratios, corresponding spins and tidal deformabilities are extracted from the posterior samples. This was used to compute the M_{disc} corresponding to each set of samples, and the results for each flavour of the posterior distribution is shown in Figs.

¹ `IMRPhenomPv2NRT` is the LAL C routine that models the phenomenological inspiral-merger-ringdown gravitational waveform for a spinning, precessing binary with numerical relativity-tuned tidal effects (see LIGO Scientific Collaboration 2018a, and Dietrich et al. 2019).

4.4 – 4.5 below.

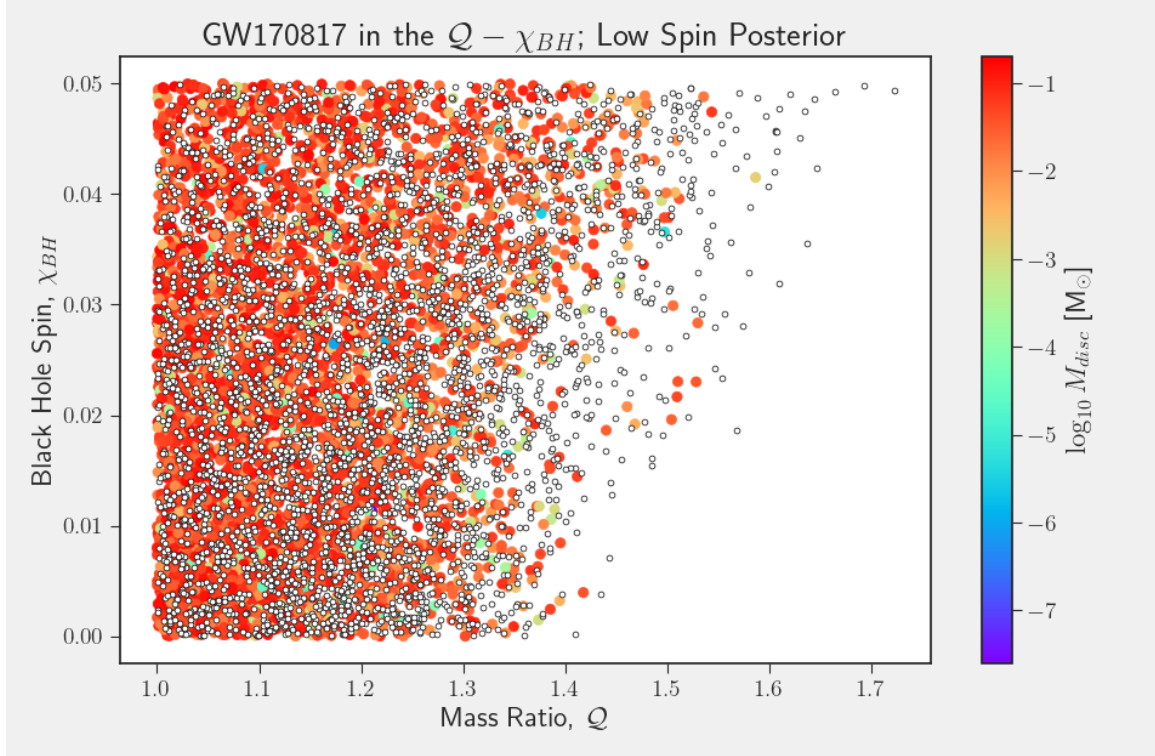


Figure 4.4: Samples from the low spin posterior distribution for GW170817, in the $\mathcal{Q} - \chi_{BH}$ plane. The color coding for a point in the plane is the M_{disc} computed for that \mathcal{Q} and χ_{BH} , and unfilled (white) circles represent posterior samples which have $M_{disc} = 0$.

As can be seen from Figs. 4.4 – 4.5, more than 50% of the posterior sample sets produce a disc mass (i.e. $M_{disc} \neq 0$), and thus can support jet launching given the right black hole spin and energy extraction conditions. Specifically, for the high-spin posterior, around 57.1% of the samples produce a disc whereas in the case of the low-spin posterior, around 55.9% of the samples produce a disc.

Furthermore, from EM follow-up observations and analysis, estimates have been obtained for the viewing angle, θ_v at which GW170817 was seen (see Finstad et al. 2018). This value has been constrained to be $\theta_v \sim 20^\circ$. Using this, the value of the apparent isotropic equivalent energies for the posterior samples is calculated, which show a median value of $E_{iso}(20^\circ) \approx 1.21 \times 10^{47}$ erg for the high-spin prior whereas the same value is $E_{iso}(20^\circ) \approx 8.06 \times 10^{46}$ erg for the low-spin prior, which is lower than the observed isotropic equivalent energies for cosmological SGRBs (see Table 3.5), but comparable with the $E_{iso}(\theta_v)$ that is obtained when treating GW170817 as

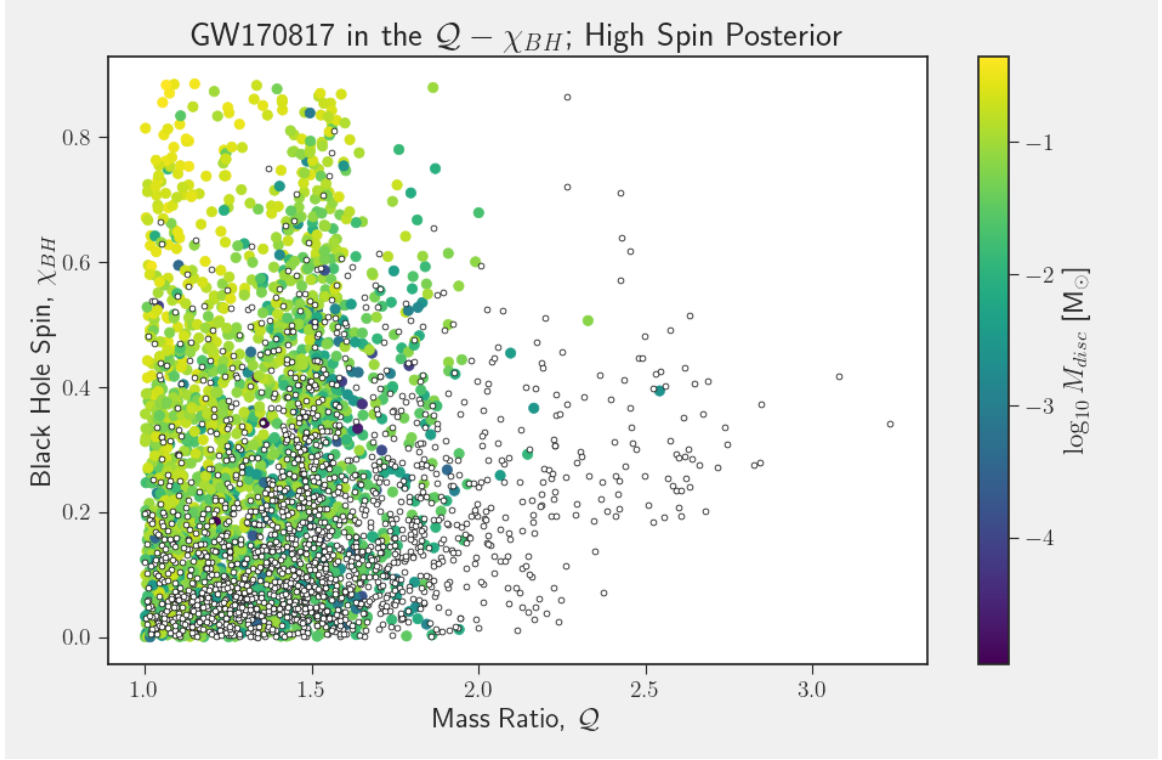


Figure 4.5: Samples from the high spin posterior distribution for GW170817, in the $Q - \chi_{BH}$ plane. The color coding for a point in the plane is computed similar to the process followed in Fig. 4.4.

a BNS merger.

4.2.3 GW190425

For completeness, the analysis carried out for GW170817 and GW190426_152155 is also carried out for GW190425. A similar process is carried out and the posteriors samples released for the component masses, component spins etc., are used to compute the disc mass using the current framework. The result of doing this analysis is shown Figs. 4.6 – 4.7.

As can be seen from these figures, most of the samples support the formation of a disc around the remnant black hole. In fact, for the high-spin posterior, around 92% of the samples have a $M_{disc} > 0$ whereas in the case of the low-spin posterior, almost 33% of the samples have a $M_{disc} > 0$. This can be interpreted as indicating the fact that it is wholly possible that 190425 was an NSBH event which launched a SGRB jet which was missed because of it being off-axis to observers on the Earth, although

the degree to which it is probable depends on the black hole spin prior distribution used.

Since there were no EM observations which would help constrain the viewing angle of the event, the apparent on-axis isotropic equivalent energy is taken as the next best measure which can shed more light on the energetics of the SGRB jet. Assuming a Gaussian structured jet, it is seen that the median value of $E_{iso}(0) \approx 3.765 \times 10^{51}$ erg for the high-spin posteriors whereas that for the low-spin posterior is $E_{iso}(0) \approx 1.607 \times 10^{51}$ erg. This puts this event in the energy range of cosmological SGRBs, further evidencing the possibility of GW190425 as a low mass BH, high mass NS merger event which led to an SGRB jet.

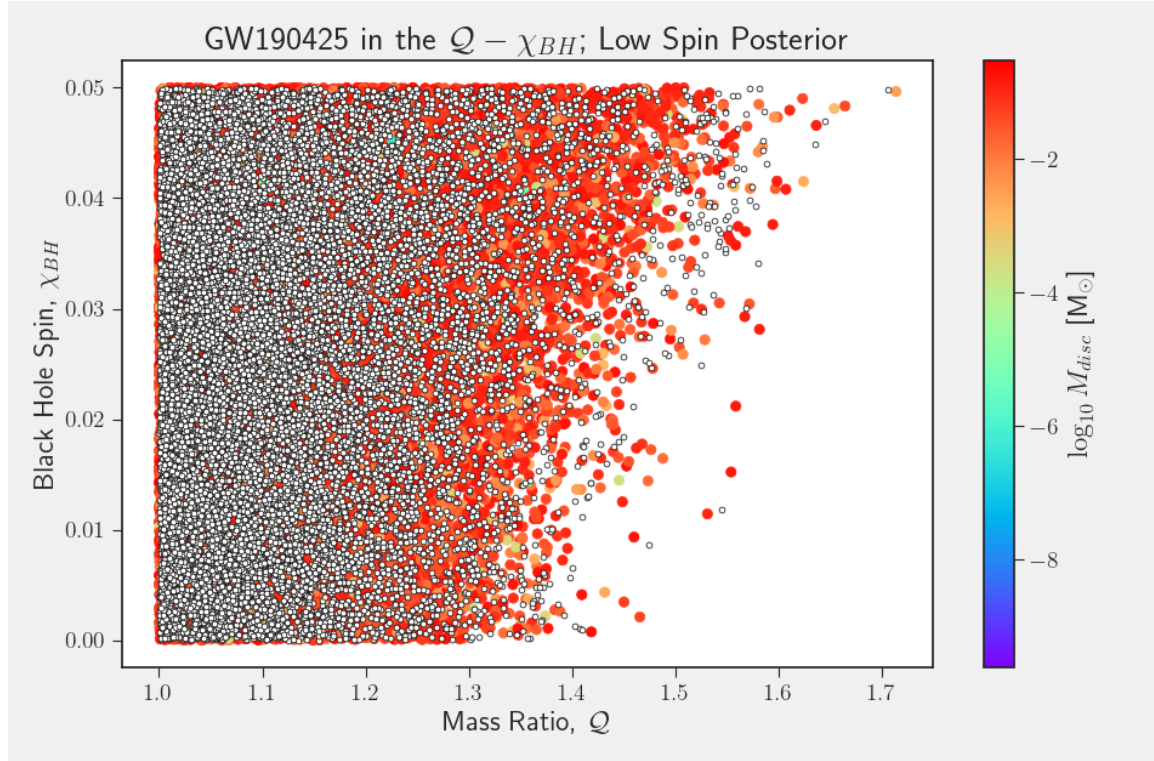


Figure 4.6: Samples from the low spin posterior distribution for GW190425, in the $\mathcal{Q} - \chi_{BH}$ plane. The color coding for a point in the plane is the M_{disc} computed for that \mathcal{Q} and χ_{BH} , and unfilled (white) circles represent posterior samples which have $M_{disc} = 0$.

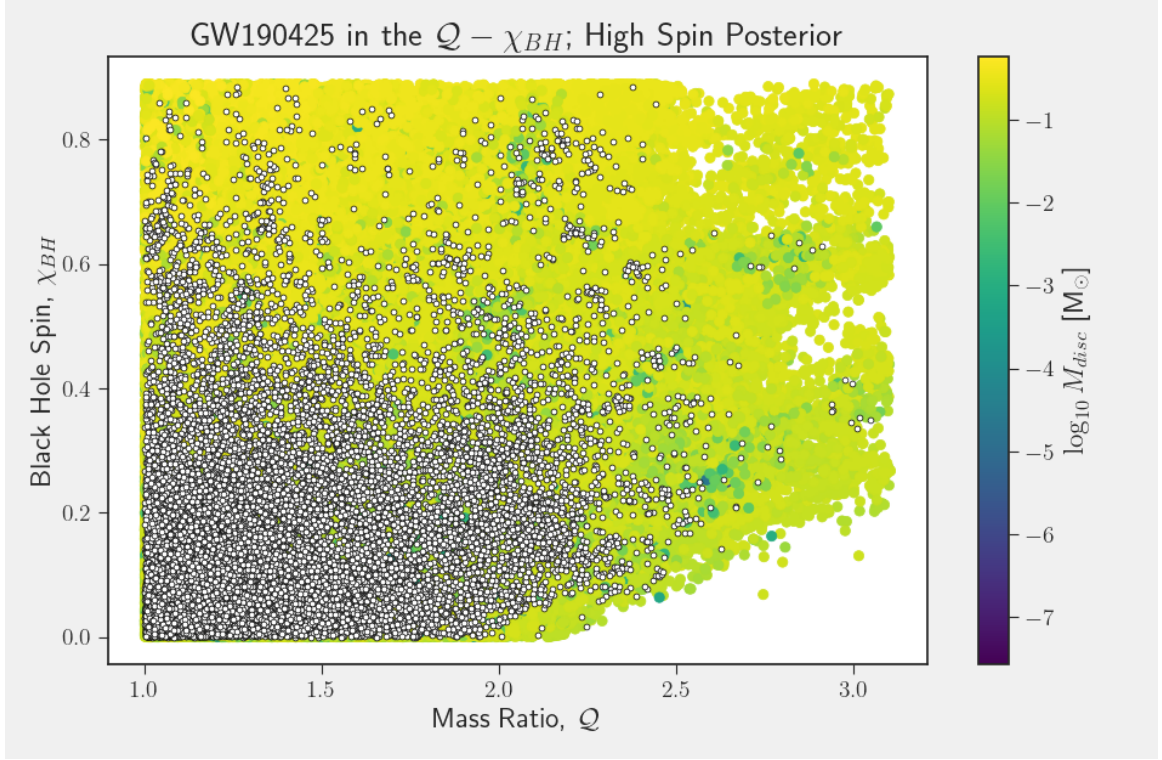


Figure 4.7: Samples from the high spin posterior distribution for GW190425, in the $Q - \chi_{BH}$ plane. The color coding for a point in the plane is computed similar to the process followed in Fig. 4.6.

4.3 Summary

In this chapter, the populations synthesized using codes described in Chapter 2 and events of interest introduced in Chapter 3 are analysed more carefully. Specifically, in the case of GW190426_152155, the hypothesis that it could have been an NSBH merger event is carefully considered under the current framework. Since it did not fit in well with the current framework, alternatives hypotheses are proposed, although more work needs to be done in terms of verifying these alternative hypotheses.

Similar analyses was also carried out for the events GW170817 and GW190425, which are currently classified as BNS mergers to a high degree of confidence, but still admit non-negligible possibility to launching a jet within the current framework.

As for the population analysis, it was ascertained that the EM outflows from NSBH mergers with the currently assumed population parameters strongly depends on the black hole spin prior distribution. In the absence of any strong indication to favour one spin distribution over another in the case of black holes in an NSBH binary, all

of these spin distributions must be considered likely. Further work needs to be done in order to take these assumptions about the spin distributions to their logical ends, and in doing so, it is hoped that multiple spin distributions would be ruled out due to incompatibility with the observational data. This is what is planned to be carried out, via the computation of the rate density of SGRBs as calculated from NSBH merger rates. This number will be an independent estimate of the SGRB rate density as calculated by EM observers, and will serve to differentiate physical from non-physical priors.

Chapter 5

Results and Discussion

5.1 Summary

References

- Abbott, B. P. et al. (Oct. 2017). “Multi-messenger Observations of a Binary Neutron Star Merger”. In: *Astrophysical Journal Letters* 848.2, L12, p. L12. DOI: 10.3847/2041-8213/aa91c9. arXiv: 1710.05833 [astro-ph.HE].
- (Oct. 2018). “GW170817: Measurements of Neutron Star Radii and Equation of State”. In: *Physical Review Letters* 121.16, 161101, p. 161101. DOI: 10.1103/PhysRevLett.121.161101. arXiv: 1805.11581 [gr-qc].
- Abbott, R. et al. (Oct. 2020). “GWTC-2: Compact Binary Coalescences Observed by LIGO and Virgo During the First Half of the Third Observing Run”. In: *arXiv e-prints*, arXiv:2010.14527, arXiv:2010.14527. arXiv: 2010.14527 [gr-qc].
- Barbieri, C., O. S. Salafia, M. Colpi, et al. (Dec. 2019). “Filling the Mass Gap: How Kilonova Observations Can Unveil the Nature of the Compact Object Merging with the Neutron Star”. In: *The Astrophysical Journal* 887.2, p. L35. DOI: 10.3847/2041-8213/ab5c1e. URL: <https://doi.org/10.3847/2041-8213/ab5c1e>.
- Barbieri, C., O. S. Salafia, A. Perego, et al. (May 2019). “Light-curve models of black hole – neutron star mergers: steps towards a multi-messenger parameter estimation”. In: *Astronomy & Astrophysics* 625, A152. DOI: 10.1051/0004-6361/201935443. URL: <https://doi.org/10.1051/0004-6361/201935443>.
- Bardeen, James M., William H. Press, and Saul A. Teukolsky (Dec. 1972). “Rotating Black Holes: Locally Nonrotating Frames, Energy Extraction, and Scalar Synchrotron Radiation”. In: *The Astrophysical Journal* 178, p. 347. DOI: 10.1086/151796. URL: <https://doi.org/10.1086/151796>.
- Biscoveanu, Sylvia, Eric Thrane, and Salvatore Vitale (Apr. 2020). “Constraining Short Gamma-Ray Burst Jet Properties with Gravitational Waves and Gamma-Rays”. In: *The Astrophysical Journal* 893.1, p. 38. DOI: 10.3847/1538-4357/ab7eaf. URL: <https://doi.org/10.3847/1538-4357/ab7eaf>.

- Borhanian, Ssohrab (Oct. 2020). “gwbench: a novel Fisher information package for gravitational-wave benchmarking”. In: *arXiv e-prints*, arXiv:2010.15202, arXiv:2010.15202. arXiv: 2010.15202 [gr-qc].
- Cutler, Curt and Éanna E. Flanagan (Mar. 1994). “Gravitational waves from merging compact binaries: How accurately can one extract the binary’s parameters from the inspiral waveform?” In: *Physical Review D* 49.6, pp. 2658–2697. DOI: 10.1103/physrevd.49.2658. URL: <https://doi.org/10.1103/physrevd.49.2658>.
- Dietrich, Tim et al. (Aug. 2019). “Improving the NRTidal model for binary neutron star systems”. In: *Physical Review D* 100.4. DOI: 10.1103/physrevd.100.044003. URL: <https://doi.org/10.1103/physrevd.100.044003>.
- Finstad, Daniel et al. (June 2018). “Measuring the Viewing Angle of GW170817 with Electromagnetic and Gravitational Waves”. In: *The Astrophysical Journal* 860.1, p. L2. DOI: 10.3847/2041-8213/aac6c1. URL: <https://doi.org/10.3847/2041-8213/aac6c1>.
- Foucart, F. et al. (May 2019). “Numerical simulations of neutron star-black hole binaries in the near-equal-mass regime”. In: *Physical Review D* 99.10. DOI: 10.1103/physrevd.99.103025. URL: <https://doi.org/10.1103/physrevd.99.103025>.
- Foucart, Francois (July 2020). “A Brief Overview of Black Hole-Neutron Star Mergers”. In: *Frontiers in Astronomy and Space Sciences* 7. DOI: 10.3389/fspas.2020.00046. URL: <https://doi.org/10.3389/fspas.2020.00046>.
- Foucart, Francois, Tanja Hinderer, and Samaya Nissanke (Oct. 2018). “Remnant baryon mass in neutron star-black hole mergers: Predictions for binary neutron star mimickers and rapidly spinning black holes”. In: *Physical Review D* 98.8. DOI: 10.1103/physrevd.98.081501. URL: <https://doi.org/10.1103/physrevd.98.081501>.
- Ghirlanda, G. et al. (Oct. 2016). “Short gamma-ray bursts at the dawn of the gravitational wave era”. In: *Astronomy & Astrophysics* 594, A84, A84. DOI: 10.1051/0004-6361/201628993. arXiv: 1607.07875 [astro-ph.HE].
- Gottlieb, Ore et al. (June 2018). “A cocoon shock breakout as the origin of the γ -ray emission in GW170817”. In: *Monthly Notices of the Royal Astronomical Society*. DOI: 10.1093/mnras/sty1462. URL: <https://doi.org/10.1093/mnras/sty1462>.

- Granot, Jonathan et al. (May 2002). “Off-Axis Afterglow Emission from Jetted Gamma-Ray Bursts”. In: *The Astrophysical Journal* 570.2, pp. L61–L64. DOI: 10.1086/340991. URL: <https://doi.org/10.1086/340991>.
- Hayes, Fergus et al. (Mar. 2020). “Comparing Short Gamma-Ray Burst Jet Structure Models”. In: *The Astrophysical Journal* 891.2, p. 124. DOI: 10.3847/1538-4357/ab72fc. URL: <https://doi.org/10.3847/1538-4357/ab72fc>.
- Hinderer, Tanja et al. (Sept. 2019). “Distinguishing the nature of comparable-mass neutron star binary systems with multimessenger observations: GW170817 case study”. In: *Physical Review D* 100.6. DOI: 10.1103/physrevd.100.063021. URL: <https://doi.org/10.1103/physrevd.100.063021>.
- Ioka, Kunihiro and Takashi Nakamura (June 2019). “Spectral puzzle of the off-axis gamma-ray burst in GW170817”. In: *Monthly Notices of the Royal Astronomical Society* 487.4, pp. 4884–4889. DOI: 10.1093/mnras/stz1650. URL: <https://doi.org/10.1093/mnras/stz1650>.
- Kapadia, Shasvath J et al. (Jan. 2020). “A self-consistent method to estimate the rate of compact binary coalescences with a Poisson mixture model”. In: *Classical and Quantum Gravity* 37.4, p. 045007. DOI: 10.1088/1361-6382/ab5f2d. URL: <https://doi.org/10.1088/1361-6382/ab5f2d>.
- Kastha, Shilpa, M Saleem, and K G Arun (Apr. 2020). “Imprints of the redshift evolution of double neutron star merger rate on the signal-to-noise ratio distribution”. In: *Monthly Notices of the Royal Astronomical Society* 496.1, pp. 523–531. DOI: 10.1093/mnras/staa1077. URL: <https://doi.org/10.1093/mnras/staa1077>.
- Kawaguchi, Kyohei et al. (June 2016). “Models of Kilonova/Macronova Emission from Black Hole–Neutron Star Mergers”. In: *The Astrophysical Journal* 825.1, p. 52. DOI: 10.3847/0004-637x/825/1/52. URL: <https://doi.org/10.3847/0004-637x/825/1/52>.
- Lazzati, Davide (Nov. 2020). “Short Duration Gamma-Ray Bursts and Their Outflows in Light of GW170817”. In: *Frontiers in Astronomy and Space Sciences* 7. DOI: 10.3389/fspas.2020.578849. URL: <https://doi.org/10.3389/fspas.2020.578849>.
- Lee, William H and Enrico Ramirez-Ruiz (Jan. 2007). “The progenitors of short gamma-ray bursts”. In: *New Journal of Physics* 9.1, pp. 17–17. DOI: 10.1088/1367-2630/9/1/017. URL: <https://doi.org/10.1088/1367-2630/9/1/017>.
- LIGO Scientific Collaboration (2018a). *LIGO Algorithm Library*. DOI: 10.7935/GT1W-FZ16. URL: <https://git.ligo.org/lscsoft/lalsuite>.

- (2018b). *Parameter estimation sample release for GWTC-1*. DOI: 10.7935/KSX7-QQ51. URL: <https://dcc.ligo.org/LIGO-P1800370/public>.
- Metzger, Brian D. (Dec. 2019). “Kilonovae”. In: *Living Reviews in Relativity* 23.1. DOI: 10.1007/s41114-019-0024-0. URL: <https://doi.org/10.1007/s41114-019-0024-0>.
- Minaev, P. et al. (Apr. 2019). *GCN #24170*. GCN Circular. URL: <https://gcn.gsfc.nasa.gov/gcn3/24170.gcn3>.
- Mohan, S, M Saleem, and L Resmi (Dec. 2019). “Detectability of Electromagnetic counterparts from Neutron Star mergers: prompt emission vs afterglow”. In: *arXiv e-prints*, arXiv:1912.09436, arXiv:1912.09436. arXiv: 1912.09436 [astro-ph.HE].
- Narayan, Ramesh, Bohdan Paczynski, and Tsvi Piran (Aug. 1992). “Gamma-ray bursts as the death throes of massive binary stars”. In: *The Astrophysical Journal* 395, p. L83. DOI: 10.1086/186493. URL: <https://doi.org/10.1086/186493>.
- Nitz, Alex et al. (May 2021). *gwastro/pycbc: PyCBC Release 1.18.1*. Version v1.18.1. DOI: 10.5281/zenodo.4849433. URL: <https://doi.org/10.5281/zenodo.4849433>.
- Pannarale, Francesco (Nov. 2013). “Black hole remnant of black hole-neutron star coalescing binaries”. In: *Physical Review D* 88.10. DOI: 10.1103/physrevd.88.104025. URL: <https://doi.org/10.1103/physrevd.88.104025>.
- Poisson, Eric and Clifford M. Will (July 1995). “Gravitational waves from inspiraling compact binaries: Parameter estimation using second-post-Newtonian waveforms”. In: *Physical Review D* 52.2, pp. 848–855. DOI: 10.1103/PhysRevD.52.848. arXiv: gr-qc/9502040 [gr-qc].
- Postnov, K. A., A. G. Kuranov, and I. V. Simkin (Nov. 2019). “Possible Electromagnetic Phenomena during the Coalescence of Neutron Star–Black Hole Binary Systems”. In: *Astronomy Letters* 45.11, pp. 728–739. DOI: 10.1134/s1063773719110045. URL: <https://doi.org/10.1134/s1063773719110045>.
- Ruiz, Milton et al. (Dec. 2020). “Black hole-neutron star coalescence: Effects of the neutron star spin on jet launching and dynamical ejecta mass”. In: *Physical Review D* 102.12. DOI: 10.1103/physrevd.102.124077. URL: <https://doi.org/10.1103/physrevd.102.124077>.
- Salafia, O. S. et al. (May 2015). “Structure of gamma-ray burst jets: intrinsic versus apparent properties”. In: *Monthly Notices of the Royal Astronomical Society* 450.4, pp. 3549–3558. DOI: 10.1093/mnras/stv766. URL: <https://doi.org/10.1093/mnras/stv766>.

- Saleem, M. et al. (Mar. 2020). “On the Energetics of a Possible Relativistic Jet Associated with the Binary Neutron Star Merger Candidate S190425z”. In: *The Astrophysical Journal* 891.2, p. 130. DOI: 10.3847/1538-4357/ab6731. URL: <https://doi.org/10.3847/1538-4357/ab6731>.
- Schutz, Bernard F. (June 2011). “Networks of gravitational wave detectors and three figures of merit”. In: *Classical and Quantum Gravity* 28.12, 125023, p. 125023. DOI: 10.1088/0264-9381/28/12/125023. arXiv: 1102.5421 [astro-ph.IM].
- Seto, Naoki (Jan. 2015). “Probability distribution function for inclinations of merging compact binaries detected by gravitational wave interferometers”. In: *Monthly Notices of the Royal Astronomical Society* 446.3, pp. 2887–2894. DOI: 10.1093/mnras/stu2183. arXiv: 1410.5136 [astro-ph.CO].
- Shibata, Masaru and Kenta Hotokezaka (Oct. 2019). “Merger and Mass Ejection of Neutron Star Binaries”. In: *Annual Review of Nuclear and Particle Science* 69.1, pp. 41–64. DOI: 10.1146/annurev-nucl-101918-023625. URL: <https://doi.org/10.1146/annurev-nucl-101918-023625>.
- The LIGO Scientific Collaboration et al. (Oct. 2020). “Population Properties of Compact Objects from the Second LIGO-Virgo Gravitational-Wave Transient Catalog”. In: *arXiv e-prints*, arXiv:2010.14533, arXiv:2010.14533. arXiv: 2010.14533 [astro-ph.HE].
- Yagi, Kent and Nicolás Yunes (Apr. 2017). “Approximate universal relations for neutron stars and quark stars”. In: *Physics Reports* 681, pp. 1–72. DOI: 10.1016/j.physrep.2017.03.002. URL: <https://doi.org/10.1016/j.physrep.2017.03.002>.
- Zhu, Jin-Ping et al. (June 2020). “Kilonova Emission from Black Hole–Neutron Star Mergers. I. Viewing-angle-dependent Lightcurves”. In: *The Astrophysical Journal* 897.1, p. 20. DOI: 10.3847/1538-4357/ab93bf. URL: <https://doi.org/10.3847/1538-4357/ab93bf>.